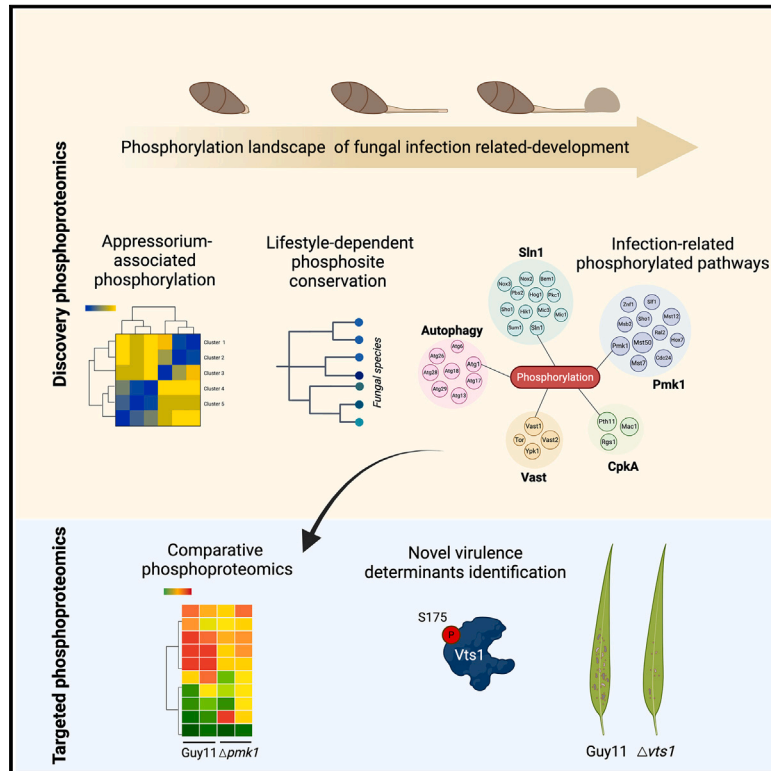


The phosphorylation landscape of infection-related development by the rice blast fungus

Graphical abstract



Authors

Neftaly Cruz-Mireles, Miriam Osés-Ruiz, Paul Derbyshire, ..., Dan MacLean, Nicholas J. Talbot, Frank L.H. Menke

Correspondence

nick.talbot@tsl.ac.uk (N.J.T.),
frank.menke@tsl.ac.uk (F.L.H.M.)

In brief

A comprehensive phosphoproteomic analysis of infection-related development by a pathogenic fungus that aims to characterize cellular signaling during plant infection to inform future disease control.

Highlights

- Phosphoproteomic landscape of infection-related development by a plant pathogenic fungus
- Conserved phosphorylation mapped in 41 fungal species with distinct pathogenic lifestyles
- Thirty-two substrates of Pmk1 identified
- Developmental regulator Vts1 requires phosphorylation by Pmk1 for its virulence activity



Resource

The phosphorylation landscape of infection-related development by the rice blast fungus

Neftaly Cruz-Mireles,¹ Miriam Osés-Ruiz,^{1,3} Paul Derbyshire,¹ Clara Jégousse,¹ Lauren S. Ryder,¹ Mark Jave A. Bautista,¹ Alice Eseola,¹ Jan Sklenar,¹ Bozeng Tang,¹ Xia Yan,¹ Weibin Ma,¹ Kim C. Findlay,² Vincent Were,¹ Dan MacLean,¹ Nicholas J. Talbot,^{1,*} and Frank L.H. Menke^{1,4,*}

¹The Sainsbury Laboratory, University of East Anglia, Norwich Research Park, Norwich NR4 7UH, UK

²Department of Cell and Developmental Biology, The John Innes Centre, Norwich Research Park, Norwich NR4 7UH, UK

³Present address: IMAB, Public University of Navarre (UPNA), Campus Arrosadia, Pamplona, Navarra 31006, Spain

⁴Lead contact

*Correspondence: nick.talbot@tsl.ac.uk (N.J.T.), frank.menke@tsl.ac.uk (F.L.H.M.)

<https://doi.org/10.1016/j.cell.2024.04.007>

SUMMARY

Many of the world's most devastating crop diseases are caused by fungal pathogens that elaborate specialized infection structures to invade plant tissue. Here, we present a quantitative mass-spectrometry-based phosphoproteomic analysis of infection-related development by the rice blast fungus *Magnaporthe oryzae*, which threatens global food security. We mapped 8,005 phosphosites on 2,062 fungal proteins following germination on a hydrophobic surface, revealing major re-wiring of phosphorylation-based signaling cascades during appressorium development. Comparing phosphosite conservation across 41 fungal species reveals phosphorylation signatures specifically associated with biotrophic and hemibiotrophic fungal infection. We then used parallel reaction monitoring (PRM) to identify phosphoproteins regulated by the fungal Pmk1 MAPK that controls plant infection by *M. oryzae*. We define 32 substrates of Pmk1 and show that Pmk1-dependent phosphorylation of regulator Vts1 is required for rice blast disease. Defining the phosphorylation landscape of infection therefore identifies potential therapeutic interventions for the control of plant diseases.

INTRODUCTION

Fungal pathogens have evolved specialized infection-related structures to penetrate the tough outer layers of plants to cause disease. These infection structures—which include appressoria, hyphopodia, and infection cushions—are important determinants of some of the most serious crop diseases, including cereal rusts and powdery mildews,^{1,2} but their biology is poorly understood. Formation of these structures requires major morphogenetic changes and remodeling of signaling transduction events, including phosphorylation. Some of these events are controlled by major regulators, such as mitogen-activated protein kinases (MAPKs). The devastating rice blast fungus *Magnaporthe oryzae*, which destroys enough rice each year to feed 60 million people, develops a melanin-pigmented appressorium that generates enormous turgor pressure of up to 8.0 MPa, which enables the pathogen to rupture the tough rice leaf cuticle.^{3,4} Appressorium morphogenesis in *M. oryzae* requires a MAPK signaling pathway in which the pathogenicity mitogen-activated kinase 1 (Pmk1) MAPK is a central component.⁵ The importance of Pmk1 is illustrated by the fact that $\Delta pmk1$ mutants are unable to form appressoria and fail to cause blast disease, while conditional inactivation of the kinase using an analog-sensitive mutant prevents invasive fungal growth in plant tissue.^{5,6}

Global transcriptional profiling has revealed that Pmk1 regulates 49% of the *M. oryzae* transcriptome during appressorium development—highlighting both its importance and the complexity of infection-related morphogenesis.⁷

Components of the Pmk1 cascade have predominantly been identified based on their counterparts in the well-known yeast Fus3/Kss1 pathway required for pheromone signaling and invasive growth.^{8,9} Upstream kinases Mst11 and Mst7, for example, were functionally characterized based on their homology to the yeast MAPKKK Ste11 and MAPKK Ste7, respectively.¹⁰ Similarly, the adaptor protein Mst50 was identified by homology to Ste50 and shown to control the activity of the three-tiered Mst11-Mst7-Pmk1 MAPK module during appressorium formation.¹¹ A limited number of downstream interactors of Pmk1 have also been identified, including transcription factors Mst12, Hox7, and Slf1,^{7,12} and the Pmk1-interacting clone Pic5.¹³ However, the molecular mechanisms through which these downstream Pmk1 signaling components regulate blast infection remain unknown.

Importantly, Pmk1 counterparts have now been identified in more than 30 fungal pathogen species, including major human, animal, and plant pathogens. In all cases so far reported, these MAPKs have been shown to be necessary for fungal pathogenicity.^{14,15} This includes the causal agents of many of the world's



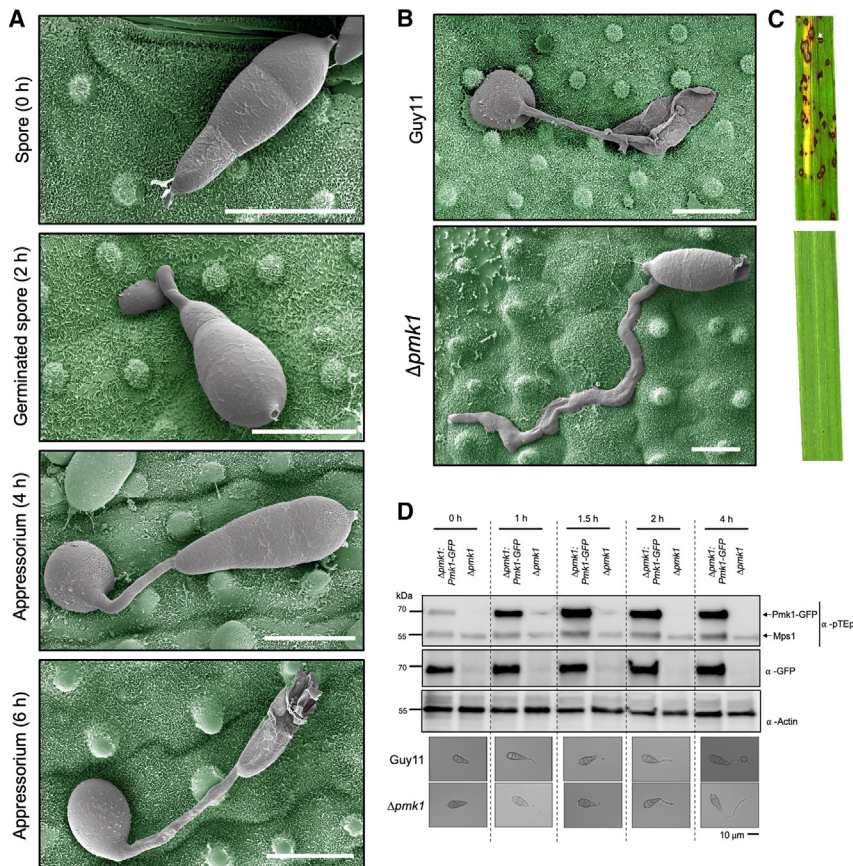


Figure 1. Early morphogenetic transitions in the appressorium overlap with activation of the Pmk1 signaling cascade

(A) Scanning electron micrographs (SEMs) with false coloring to show appressorium germination of wild-type strain Guy11 at 0, 2, 4, and 6 h.

(B) SEM with false coloring to show appressorium germination of Guy11 and $\Delta pmk1$ strains at 24 h. In (A) and (B), the blast fungus is shown in gray, and rice leaf surface is false-color-imaged to green. Scale bars indicate 10 μ m.

(C) Rice leaves infected with Guy11 (top) and $\Delta pmk1$ (bottom) strains. Rice seedlings of cultivar CO-39 were spray inoculated with conidial suspensions of equal concentrations of each strain and incubated for 5 days.

(D) Western blot analysis of total protein extracted from *in vitro* germinated spores at 0, 1, 1.5, 2, and 4 h from $\Delta pmk1$, complemented with *PMK1-GFP* and $\Delta pmk1$, using α -pTEpY (top), α -GFP (middle), and α -actin (lower). α -pTEpY has been also reported to detect the MAPK Mps1.²⁰ Proteins were immunoblotted with appropriate antisera (listed on the right). Arrows indicate expected band sizes.

most significant crop diseases, including Septoria blotch of wheat, southern corn leaf blight, and Fusarium head blight,¹⁶ and encompasses fungal pathogens exhibiting biotrophic, hemibiotrophic, and necrotrophic interactions. Therefore, a common feature of very diverse fungal pathogens, irrespective of whether they cause invasion of living plant tissue or destructive activity to kill plant cells, is their dependence on Pmk1-related MAPK pathways to regulate invasive growth. Collectively, these studies suggest that the Pmk1 MAPK signaling pathway may be a conserved pathway associated with fungal invasive growth that has diversified among distinct groups of pathogens. However, there is little direct evidence for this proposition because the substrates of Pmk1-related MAPKs are largely unknown in any fungal pathogen studied to date.

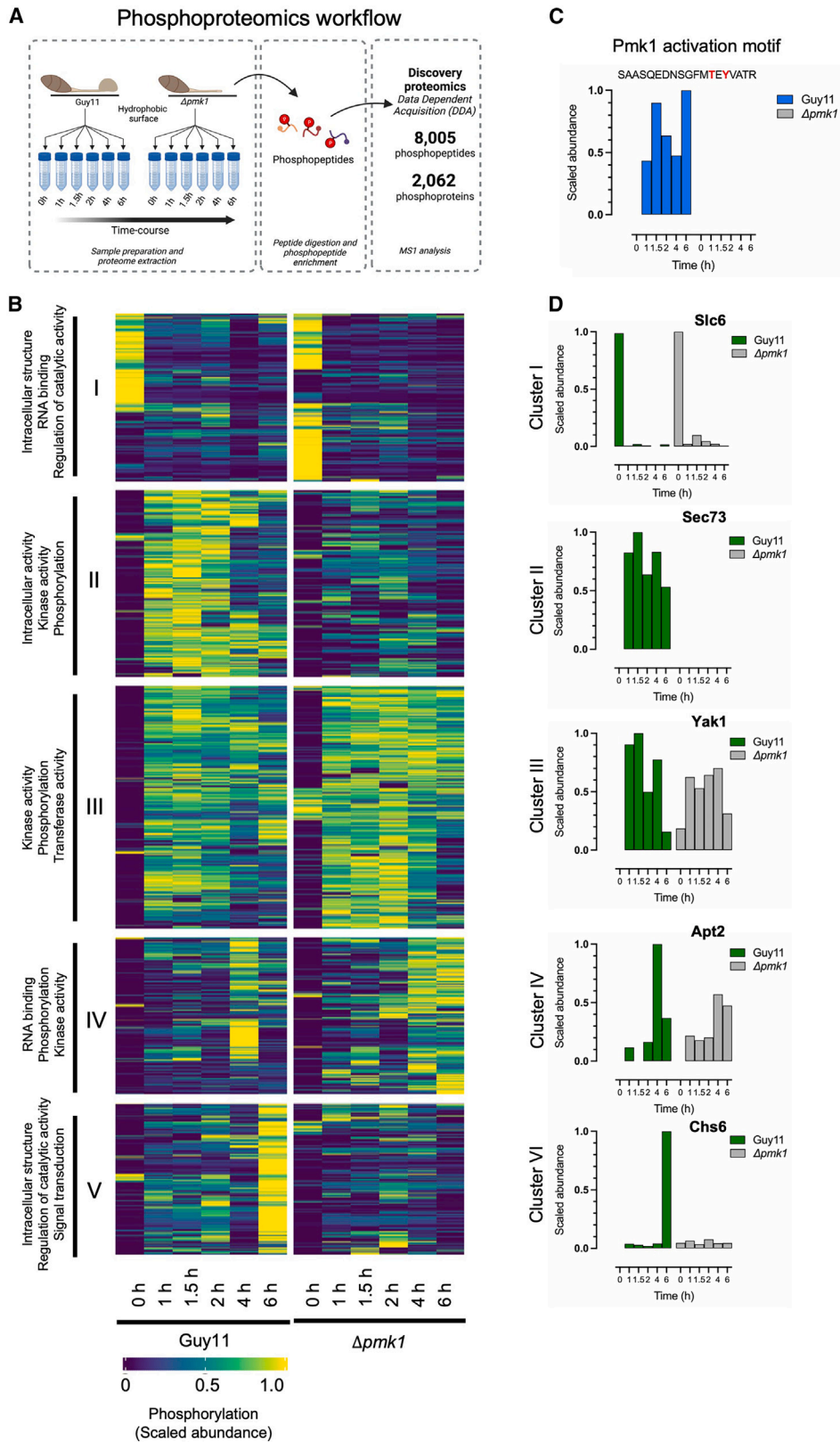
In this study, we decided to take advantage of recent advances in quantitative mass spectrometry (MS) to analyze the global pattern of phosphorylation¹⁷ during infection-related development of *M. oryzae*. We set out to define the phosphorylation signature of MAPK signaling¹⁸ associated with plant infection by fungal pathogens and identify the cellular signaling pathways regulated by Pmk1.¹⁹ Here, we report the phosphorylation landscape of appressorium morphogenesis by the blast fungus and define the major changes in phosphorylation that occur during fungal development. We use this resource to identify conserved phosphosites specific to fungal pathogens that elaborate diverse infection structures and that

exhibit distinct modes of fungal pathogenesis—including biotrophic, hemibiotrophic, and necrotrophic species—thereby defining the putative patterns of MAPK signaling across 40 major disease-causing fungal species. To validate this approach, we identified 201 phosphosites and classified them into signaling pathways and physiological processes required for infection by the blast fungus and used parallel reaction monitoring (PRM) to identify 32 putative Pmk1 substrates. This analysis enabled the identification of a regulator of appressorium morphogenesis, Vts1, which requires Pmk1-dependent phosphorylation to fulfill a key role in rice blast disease. When considered together, this study provides the most comprehensive analysis of infection-phosphorylation by a fungal pathogen to date and highlights how phosphoproteomic analysis can provide unprecedented insight into the biology of fungal invasive growth.

RESULTS

The Pmk1 MAPK is activated during infection-related development by *M. oryzae*

We first set out to define a time course for global phosphoproteomic analysis of infection-related development by the blast fungus by identifying the precise time of Pmk1 MAPK activation. Plant infection by *M. oryzae* is initiated when a fungal spore, called a conidium, lands on a hydrophobic surface and germinates to produce a polarized germ tube within 2 h (Figure 1A). By 4 h, an incipient appressorium is formed, and the contents of the conidium are recycled by autophagy to allow development of the appressorium (Figures 1A and 1B). The Pmk1 MAPK is essential for both appressorium development and virulence,⁵ and $\Delta pmk1$ mutants are unable to form appressoria and



(legend on next page)

cannot infect rice plants (Figures 1B and 1C). To investigate the temporal dynamics of Pmk1 activation, we germinated spores on an artificial hydrophobic surface that mimics the host leaf surface. We extracted protein from synchronized infection structures from the wild-type (WT) *M. oryzae* strain Guy11 and an isogenic $\Delta pmk1$ mutant. We observed that Pmk1 is phosphorylated on its TEY motif within 1 h of conidial germination on a hydrophobic surface (Figures 1A and 1D) and remains active for up to 4 h. Pmk1 activation therefore precedes infection-related development but is maintained throughout appressorium morphogenesis.

Infection-related development coincides with large changes in the phosphoproteome

To define the phosphorylation landscape of infection-related development by *M. oryzae*, we incubated conidia of Guy11 and the $\Delta pmk1$ mutant on a hydrophobic surface and performed a large-scale quantitative phosphoproteomics experiment, extracting phosphoproteins from synchronized infection structures at 0, 1, 1.5, 2, 4, and 6 h post germination (Figures 2A and S1). Using discovery proteomics based on data-dependent acquisition (DDA), we identified 8,005 phosphopeptides from 2,062 proteins from 3 biological replicates during the 6-h time course in both strains (Figures 2A and 2B). We quantified this dataset using a label-free MS1-quantification approach (LFQ) and were able to quantify 7,048 phosphopeptides (Data S1). To identify differential phosphopeptides, we determined the ratio between Guy11 time points compared with conidia ($t = 0$) and filtered for 2-fold change and an adjusted $p \leq 0.05$. With these settings, the abundance levels of 5,058 phosphopeptides were found to be significantly different during germling (1, 1.5, and 2 h) and appressoria (4 and 6 h) stages compared with conidia (0 h) in Guy11. As early as 1 h after germination, we identified large changes in abundance of phosphopeptides (420 less abundant and 2,049 more abundant) and phosphoproteins (100 less abundant and 497 more abundant) (Data S1). We have previously shown that during appressorium development, up to 50% of the transcriptome changes when compared with levels in conidia.⁷ This is mirrored by the changes in levels of all proteins identified, with at least three peptides in our dataset, including a limited subset of non-phosphorylated proteins (Data S2). The phosphorylation landscape of the emerging germling therefore undergoes significant changes due to a combination of changes in the amount of each protein as well as differential phosphorylation. Consistent with our immunoblot analysis of Pmk1 phosphorylation (Figure 1D), we can detect phosphorylation of the TEY motif in the

activation loop of Pmk1 as early as 1 h after germination, peaking at 1.5 h and remaining at a sustained level up to 4 h, and this phosphorylation was absent in the $\Delta pmk1$ mutant, as expected (Figure 2C). At 6 h, TEY phosphorylation increases again, suggesting that a second Pmk1 activation event occurs between 4 and 6 h, when the appressorium develops and a significant change in growth polarity occurs. As expected, in the $\Delta pmk1$ mutant, we cannot detect phosphorylation of the TEY motif at any time point. During the first 2 h, the number of upregulated phosphopeptides in $\Delta pmk1$ is significantly lower (1,681) compared with the WT, while the number of downregulated phosphopeptides is significantly higher (727), consistent with the absence of Pmk1 activity (Figure 2C). K-means clustering of the data revealed 5 clusters enriched for differential phosphopeptides in conidia (cluster I), germinated conidia (cluster II and cluster III), and incipient appressoria (cluster IV and cluster V) (Figure 2B). Changes in overall phosphopeptide abundance are similar for Guy11 and the $\Delta pmk1$ mutant in clusters I, III, and IV, while the abundance changes in clusters II and V are drastically different between Guy11 and $\Delta pmk1$. The absence or significant reduction in phosphopeptide abundance in the $\Delta pmk1$ background is consistent with high Pmk1 activity in Guy11 at those times. Gene Ontology (GO) term enrichment analysis for 4 of these clusters revealed biological processes and molecular functions related to signal transduction and protein phosphorylation (Figure S1). Although cluster I is enriched for intracellular anatomical structures, RNA binding proteins associated with plasma membrane and cation transport but not signal transduction or protein phosphorylation. This indicates that protein phosphorylation is one of the key primary processes during infection-related development. GO terms related to other processes known to be essential for appressorium development in *M. oryzae* are also enriched, such as autophagy (cluster II), lipid binding and actin binding (cluster III), and microtubule and intracellular transport (cluster IV).^{21–24} Cluster I represents phosphopeptides derived from proteins that are present in conidia and show lower relative abundance during the course of infection-related development. These include proteins such as the putative solute carrier transporter Slc6 (MGG_05433) (Figure 2D), glycerate-3-kinase (MGG_06149), linolate diol synthase LDS1 (MGG_10859), and eukaryotic translation initiation factor 3 subunit a (MGG_10192) (Figure S1), most of which have been shown to have a function in virulence in *M. oryzae*,^{25,26} but which represent proteins involved in metabolic functions rather than signaling. Cluster III represents proteins phosphorylated early during appressorium development with high relative abundance

Figure 2. Infection-related development causes major changes in protein phosphorylation

(A) Schematic to show the infection-related development experiment in a pathogenic (Guy11) and non-pathogenic ($\Delta pmk1$) *M. oryzae* strain. Spores and germinated cells were synchronized at 0, 1, 1.5, 2, 4, and 6 h. Phosphopeptides were enriched using TiO₂ microspheres and were subjected to liquid chromatography-tandem mass spectrometry (LC-MS/MS). Samples from 3 biological replicates were analyzed in data-dependent acquisition (DDA) mode to be quantified using label-free quantification based on precursor ions (MS1).

(B) Heatmap to show the differentially phosphorylated phosphopeptides in Guy11 and $\Delta pmk1$. Each row corresponds to a single phosphosite, and rows are ordered by hierarchical clustering (I–V). The top three GO terms for each cluster are indicated. See also Data S1.

(C) Bar graphs to show relative phosphorylation abundance for the peptide containing the Pmk1 activation motif (pTEpY) during early infection.

(D) Relative phosphorylation for representative phosphopeptides in each defined cluster. Cluster I, solute carrier family protein Slc6 (MGG_05433); cluster II, Sec73 (MGG_06905); cluster III, Yak1 (MGG_06399); cluster IV, Apt2 (MGG_07012), and cluster V, chitin synthase 6 (CH6) (MGG_13013). Data shown in (B)–(D) are based on 3 biological replicates.

See also Figure S1.

of the corresponding phosphopeptides between 1 and 4 h in both Guy11 and the $\Delta pmk1$ mutant, including the Yak1 kinase (MGG_06399) (Figure 2D) and protein phosphatase Ssd1 (MGG_08084), both of which are required for virulence.^{27,28} Phosphopeptides in cluster II show a similar relative abundance at early time points in Guy11 but little to no increase in abundance in the $\Delta pmk1$ mutant, suggesting that the corresponding proteins require Pmk1 for their phosphorylation or expression. Examples of phosphopeptides showing this type of pattern include peptides from protein transporter Sec73 (MGG_06905) (Figure 2D) and kinases Sch9 (MGG_14773) and Atg1 (MGG_06393) (Figure S1). Cluster IV and V represent phosphopeptides with high relative abundance at the time when appressorium begins to form, and these include the aminophospholipid translocase Apt2 (MGG_07012), which is essential for plant infection²⁹; the transcription factor Hox7 (MGG_12865), implicated in appressorium morphogenesis⁷; chitin synthase Chs6 (MGG_13013); and the glucosamine-6-phosphate isomerase (MGG_00625). The latter two proteins represent cluster V, which again shows phosphopeptides with high abundance at 6 h in Guy11 but mostly absent from the $\Delta pmk1$ mutant, consistent with Pmk1-dependent phosphorylation or expression. Taken together, these results show that during infection-related development by the blast fungus, major changes in the phosphoproteome landscape are occurring, including many proteins known to be required for virulence, and a subset of these phosphoprotein changes require the presence of the Pmk1 kinase.

Distinct patterns of phosphosite conservation are evident across fungal species showing diverse modes of pathogenesis

Given that we identified extensive changes in phosphorylation during infection-related development by *M. oryzae*, we decided to investigate the extent of phosphosite conservation across different fungal species. Functionally important phosphorylation sites have been proposed as likely to be conserved across multiple species^{17,30,31}; therefore, we set out to test this hypothesis in the context of fungal pathogenesis. Using Orthofinder, we identified orthogroups for 41 filamentous fungal species, including saprophytes, mutualists, plant pathogens, and human pathogens, as well as *Saccharomyces cerevisiae* and *Schizosaccharomyces pombe*, the two model yeast species (Data S3). We then mapped the conservation of all our identified *M. oryzae* phosphorylated residues onto the orthogroups for all 41 fungal species, *k*-means clustered them, using the elbow method according to the subset of species in which residues were conserved, and visualized the data in a heatmap containing 9 conserved phosphorylated residue (CPR) groups (Figure 3). We identified a total of 1,198 CPRs. Clustering species based on the conservation of phosphorylated residues (Figure 3A) results in a tree composed of distinct clades, when compared with a phylogenetic tree based on the orthogroups (Figure 3C). This provides evidence that a large proportion of the conservation of phosphorylated residues observed cannot be explained by protein conservation at the amino acid level or phylogenetic distance between species. The heatmap shows several interesting CPR clusters, of which cluster 4 likely represents core signaling proteins and CPRs observed in the majority of fungal

species (Figure 3B). Consistent with this, the cluster includes 69 proteins of which 15 are annotated as protein kinases, including the MAPKs Pmk1 and Osm1 and the MAPKK Mst7. Interestingly, CPR cluster 9 shows conservation of phosphorylated residues among the majority of plant pathogenic species but only limited conservation in saprophytes such as *Aspergillus nidulans*, *A. fumigatus*, and *A. flavus*, suggesting that these residues are associated with a lifestyle dependent on plant hosts. As expected, these two clusters show a strong correlation with a requirement for a Pmk1 MAPK ortholog for virulence/pathogenicity (Data S3). CPR cluster 6 shows a strong correlation with 16 mainly hemibiotrophic plant pathogenic fungal species; hemibiotrophic species are those that invade living plant tissue initially in their life cycle before killing plant cells at later stages of development. This includes many of the most important crop-disease-causing fungi, such as *M. oryzae* and *Zymoseptoria tritici*, and reveals phosphosite conservation in at least 13 transcription factors and a wide range of metabolic enzymes (Data S3). Cluster 3 stands out because it appears tightly associated with the genus *Fusarium*, including the wheat head blight pathogen *Fusarium graminearum*, for example, and also shows phosphosite conservation in pH-responsive and morphogenetic transcriptional regulators. Cluster 5 shows high levels of conservation among Dothideomycete pathogens, including the causal agent of new blotch of barley (*Pyrenophora teres*), brown spot of rice (*Bipolaris oryzae*), and southern corn leaf blight (*Cochliobolus heterostrophus*). The conservation of phosphosites within this group of related cereal pathogens provides evidence that the regulation of invasive growth may be similarly configured to *M. oryzae*. Finally, cluster 2 shows phosphosites conserved solely among fungi producing pressurized, melanin-pigmented appressoria, such as the *Colletotrichum* anthracnose pathogens, and—consistent with this—shows phosphosite conservation in a range of proteins previously implicated in appressorium morphogenesis (Data S3). When considered together, this comparative analysis provides evidence that subsets of the identified phosphorylated residues in *M. oryzae* are conserved among diverse pathogens, showing some common lifestyle features, such as plant association, invasive growth in living plant tissue, and the formation of specialized infection structures, providing a key resource for defining the signaling mechanisms that govern fungal pathogenesis.

Phosphorylation of signaling pathways controlling infection-related development

To investigate the relevance of the observed patterns of phosphorylation on infection-related development, we mapped 201 differentially phosphorylated residues identified by LFQ onto proteins in signaling pathways implicated in appressorium morphogenesis and plant infection. Out of 17 proteins associated with the Pmk1 MAPK signaling pathway, 11 proteins show abundance changes for 1 or more phosphopeptides, including proteins acting upstream of Pmk1, such as the MAPKK Mst7 and adaptor protein Mst50,^{10,11,32,33} as well as potential and verified downstream Pmk1 targets, such as transcription factors Sfl1, Znf1, Hox7, and Mst12.^{7,12,34,35} (Figure 4A). This high proportion of infection-regulated phosphoproteins is not limited to the Pmk1 pathway because 12 out of 25 proteins mapped onto the Sln1 histidine kinase

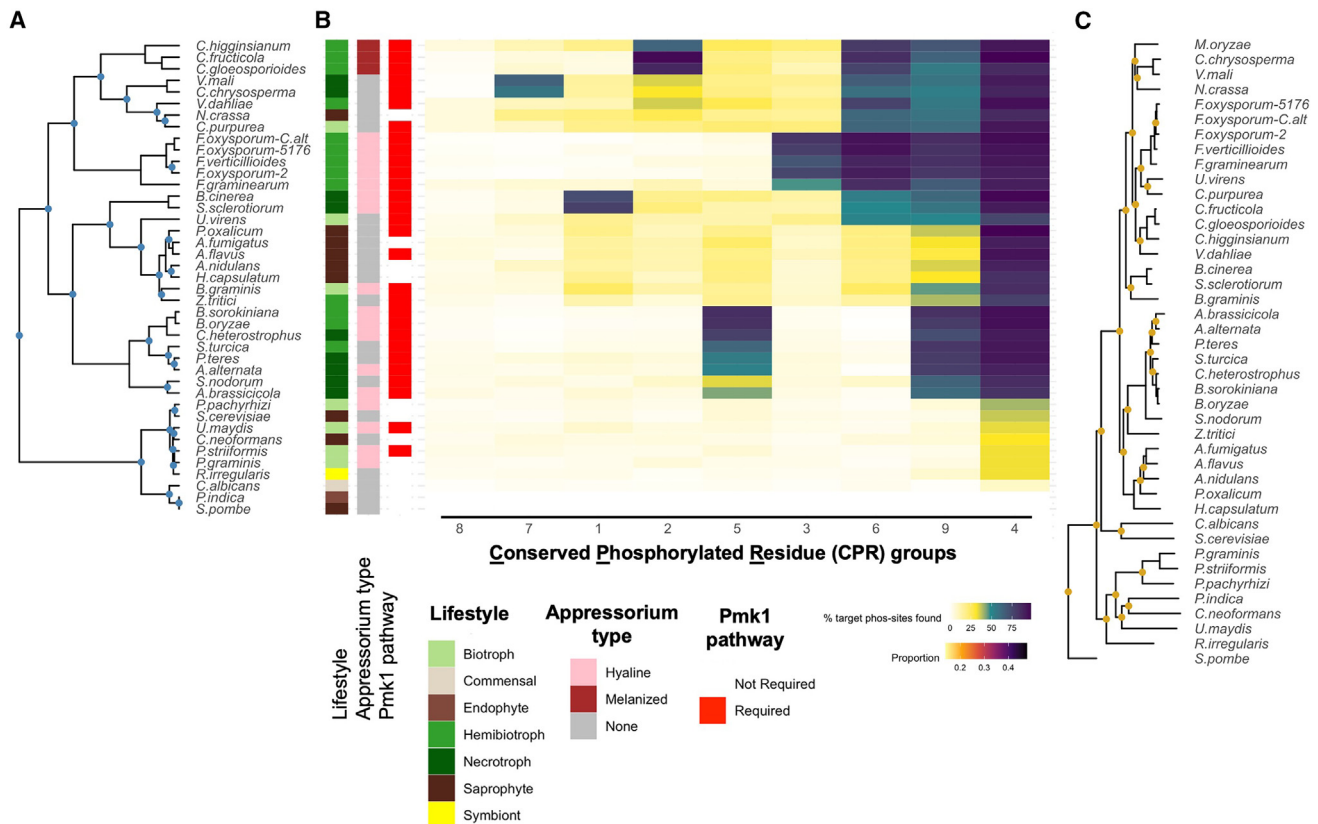


Figure 3. Evolutionary analysis determines appressorium-specific phosphosites across fungal species

(A) Fungal species tree based on the conservation of phosphorylated residues. Nodes highlighted in blue are only seen in the phosphosite conservation tree and not in the orthogroup tree shown in (C).

(B) Heatmap to show *k*-means clustered conserved phosphorylated residues among 41 fungal species from the infection-related development dataset in *M. oryzae*. Each row corresponds to a single species, and rows and columns are ordered by hierarchical clustering in 9 conserved phosphorylated residue (CPR) groups. Color indicates the percent of target phosphosites from *M. oryzae* found in other species. See also [Data S3](#).

(C) Phylogenetic tree based on the orthogroups for the 41 fungal species: *Alternaria alternata*, *Alternaria brassicicola*, *Aspergillus flavus*, *Aspergillus fumigatus*, *Aspergillus nidulans*, *Bipolaris oryzae*, *Bipolaris sorokiniana* (*Cochliobolus sativus*), *Blumeria graminis*, *Botrytis cinerea*, *Candida albicans*, *Claviceps purpurea*, *Cochliobolus heterostrophus*, *Colletotrichum fructicola*, *Colletotrichum gloeosporioides*, *Colletotrichum higginsianum*, *Cryptococcus neoformans*, *Cytospora chrysosperma*, *Fusarium graminearum*, *Fusarium oxysporum-2*, *Fusarium oxysporum-5176*, *Fusarium oxysporum-C.alt*, *Fusarium verticillioides*, *Histoplasma capsulatum*, *Neurospora crassa*, *Penicillium oxalicum*, *Phakopsora pachyrhizi*, *Piriformospora indica*, *Puccinia graminis*, *Puccinia striiformis*, *Pyrenophora teres*, *Rhizoglyphus irregularis*, *Saccharomyces cerevisiae*, *Schizosaccharomyces pombe*, *Sclerotinia sclerotiorum*, *Setosphaeria turcica*, *Stagonospora nodorum*, *Ustilago maydis*, *Valsa mali*, *Verticillium dahliae*, and *Zyoseptoria tritici*. Nodes highlighted in yellow are only seen in the ortho group tree and not seen in the phosphosite conservation tree shown in (A). See also [Figure S2](#).

signaling pathway, required for appressorium turgor sensing,³ show phosphopeptide abundance changes over the 6-h time course of infection-related development ([Figures 4D and S3](#)). Autophagy is known to be required for appressorium function and dependent on Pmk1.^{21,36} Out of 23 proteins involved in autophagy, 8 proteins associated with initiation and selective autophagy show abundance changes on one or more phosphopeptides ([Figures 4E and S3](#)). In the cyclic AMP (cAMP) protein-kinase-A-dependent signaling pathway, which acts in concert with Pmk1 to regulate initiation of appressorium development and turgor generation, 3 proteins show change in phosphoprotein levels ([Figures 4B and S3](#)). At the same time, the recently described Vast1 pathway, implicated in the control of appressorium maturation, has 4 of 5 Vast1 phosphoproteins changing in abundance,

predicting that this pathway is key to plant infection ([Figures 4C and S3](#)). In all of the signaling pathways analyzed, the phosphopeptide abundance profiles are distinct between Guy11 and the $\Delta pmk1$ mutant, providing evidence that Pmk1 plays a role in their direct or indirect regulation and highlighting the global nature of its regulatory effect on physiological and morphogenetic processes necessary for elaboration of a functional appressorium.

Targeted phosphoproteomics defines potential targets of the Pmk1 MAPK

Given the importance of Pmk1 in regulation of proteins required for plant infection by *M. oryzae*, we decided to identify direct substrates of the MAPK. For this purpose, we carried out targeted quantitative phosphoproteomic analysis in *M. oryzae*

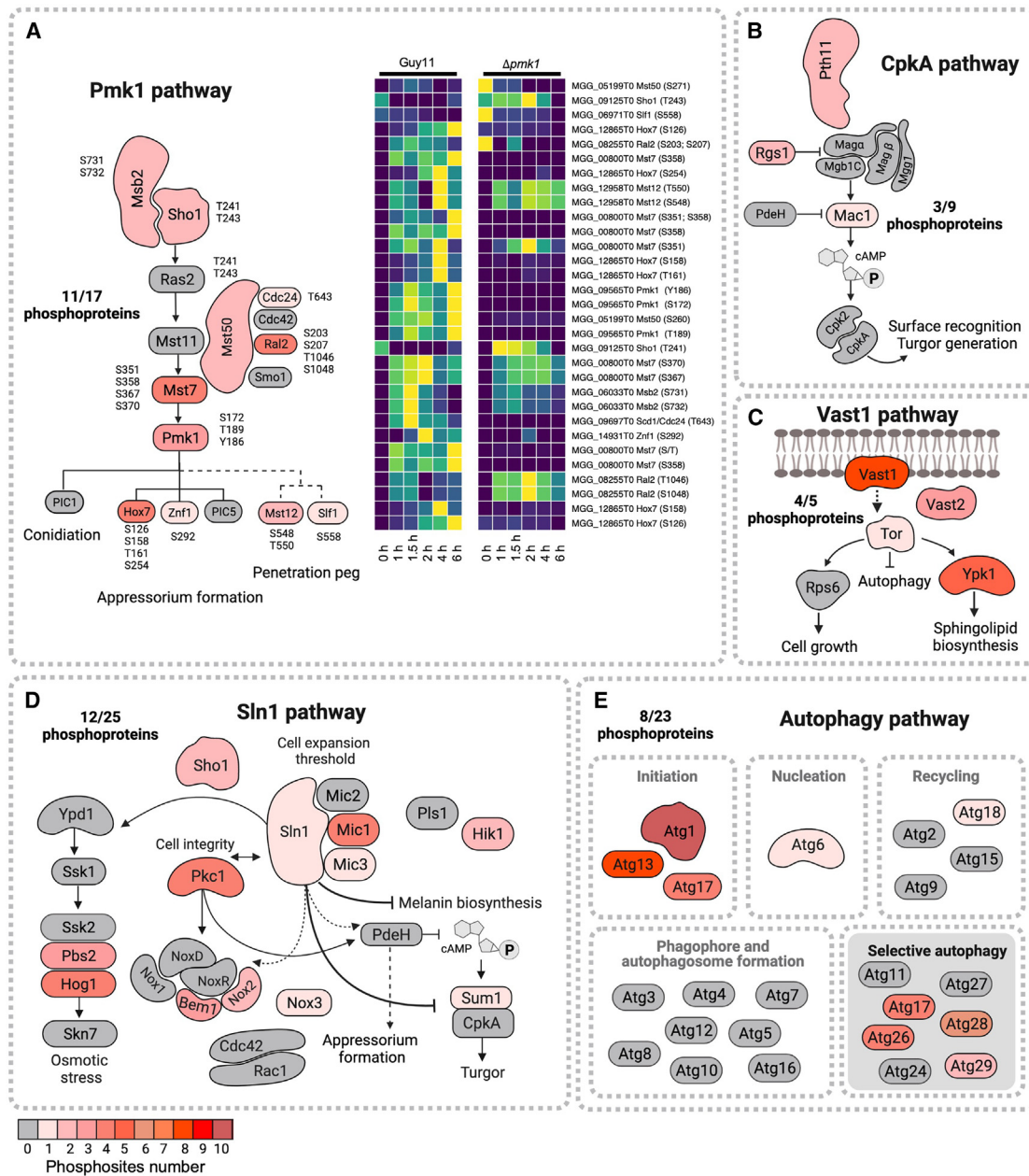


Figure 4. Phosphorylation is a major modification in proteins from pathways that control infection-related development

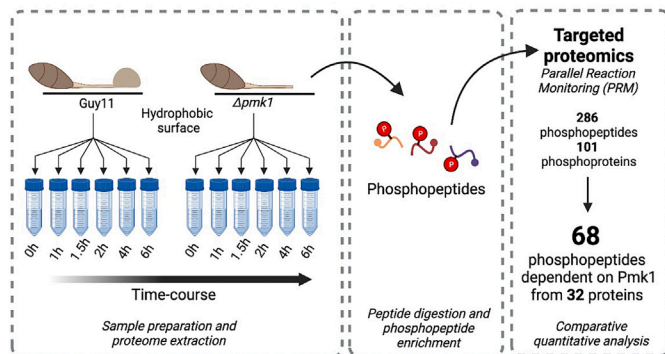
(A) On the left, schematic representation of components of the Pmk1 signaling pathway in *M. oryzae*. Differentially phosphorylated residues are indicated for each protein ($p \leq 0.05$). On the right, heatmap to show the differentially phosphorylated phosphopeptides in Guy11 and $\Delta pmk1$ during infection-related development. Each row corresponds to a single phosphosite. Data shown in the heatmap represent the average from 3 biological replicates.

(B–E) Schematic representation of components of (B) CpkA, (C) Vast1, (D) Sln1, and (E) autophagy pathways. For all represented proteins, the number of differentially phosphorylated residues is represented in red. See also [Figure S3](#).

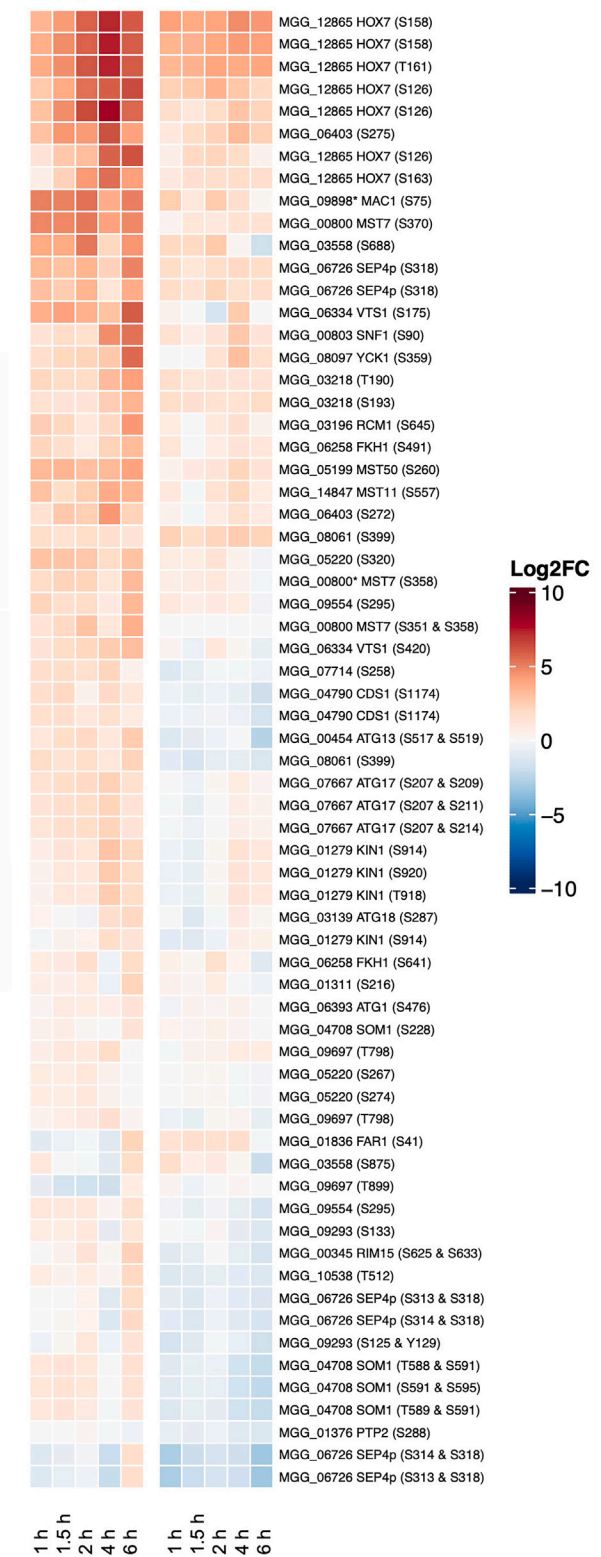
Guy11 and the $\Delta pmk1$ mutant by PRM on the same phosphopeptide-enriched samples. We used this separate, more accurate approach to enhance confidence in the identification of differential abundance of phosphopeptides as well to benchmark the LFQ data ([Data S4](#)). We hypothesized that potential direct targets of Pmk1 would be phosphorylated only in the presence of Pmk1. For PRM, we selected peptides to target from a DDA

library using the following criteria: (1) differentially phosphorylated peptides based on LFQ from both Guy11 and $\Delta pmk1$; (2) peptides from previously reported Pmk1 target proteins; and (3) potential components of the Pmk1 pathway based on a hierarchical transcriptomic analysis.⁷ Using this information, we selected a list of 286 phosphopeptides belonging to 101 proteins ([Figure 5A](#); [Data S5](#)). Of the 286 phosphopeptides quantified by

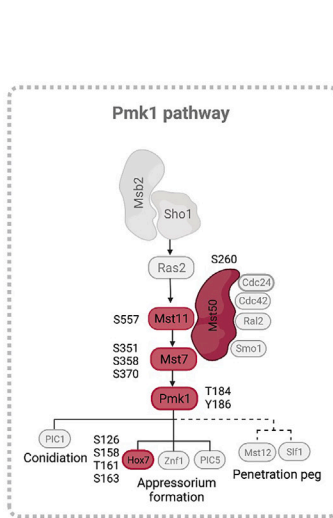
A Phosphoproteomics workflow



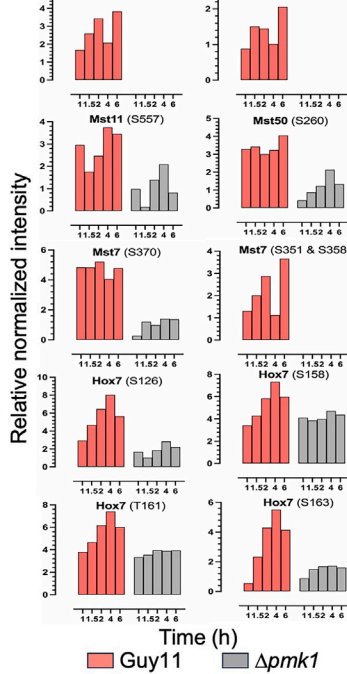
B Guy11 Δpmk1



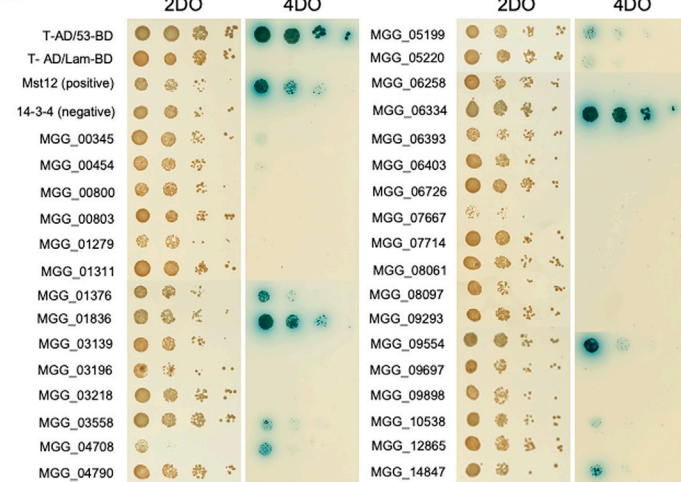
C



D



E



(legend on next page)

PRM, 182 showed differential abundance compared with conidia in one or both genotypes, representing 86 proteins (fold change: $-1 < \log_2(\text{FC}) > 1$; $p \leq 0.05$) (Figure S4). Of the 182 phosphopeptides showing differential abundance, 63 peptides from 32 proteins were differentially phosphorylated at one or more time points in Guy11 and non-differentially phosphorylated in the $\Delta pmk1$ mutant (Figure 5B). We named these proteins “putative targets of Pmk1.” Importantly, using this approach, we identified some previously reported Pmk1 targets. For example, we observed Pmk1-dependent phosphosites at S126 and S158 in the transcription factor Hox7 (Figures 5C and 5D), consistent with a previous Hox7 study.⁷ Additionally, important components of the Pmk1 pathway, such as the MAPKKK Mst11, MAPKK Mst7, and adaptor protein Mst50, also showed Pmk1-dependent phosphorylation (Figures 5C and 5D). In total, our PRM analysis of a time series study of infection-related development in *M. oryzae* identified a set of 32 putative substrates of Pmk1.

The identified potential Pmk1 targets are broadly representative of cellular processes implicated in appressorium morphogenesis, based on previous studies,⁷ but have diverse functions. Based on the MagnaGenes database of gene functional studies in *M. oryzae*,³⁷ the functions of 22 of the putative Pmk1 targets have already been studied in the blast fungus, and 19 of these are linked to infection-related development or virulence (Table 1). However, 11 proteins of this subset of putative Pmk1 targets have not yet been described. Using GO annotation, we assigned a function to each of these proteins where possible. From the proteins previously studied in *M. oryzae*, we found 5 kinases, 4 transcription factors, 1 transcriptional regulator, and 1 phosphatase. Additionally, we also found 5 autophagy-related proteins, 5 components of the Pmk1 cascade, 2 components of the cAMP signaling pathway, and 1 cytoskeleton-related protein. To determine which proteins might be direct targets of Pmk1, we carried out yeast-two-hybrid (Y2H) screening for these 32 putative targets using Pmk1 as bait on high stringency selection media (quadruple drop-out medium) (Figure 5E). We observed direct protein-protein interactions with Pmk1 in 9 of the 32 putative targets. Interactors include the transcription factors Far1,⁴⁴ implicated in the regulation of lipid metabolism associated with appressorium turgor generation and Som1, which links cell cycle control of appressorium morphogenesis with cAMP signaling,^{47,50} as well as Mst50 and Mst11, the phosphatase Ptp2, and a set of previously uncharacterized proteins, including a potential regulatory protein called

Vts1 (VT1-1-2 suppressor). Taken together, these results show that quantitative comparative phosphoproteomics can identify putative direct targets of the Pmk1 MAPK.

Vts1 is a novel component of the Pmk1 MAPK pathway during rice blast disease

To test the utility of our quantitative phosphoproteomic approach to identify novel Pmk1 targets, we decided to investigate whether Vts1 is a direct phosphorylated target of Pmk1 during appressorium development. To do this, we first tested whether Pmk1 associated with Vts1 *in vivo*. We found that Vts1 is able to interact strongly with Pmk1 in a stringent Y2H assay (Figure 5E). To show whether this interaction occurred during appressorium development, we carried out a co-immunoprecipitation experiment in appressorial protein extracts. We found that Pmk1 associates with Vts1 after 4 h during appressorium development, suggesting a possible role during development (Figure 6A). From PRM analysis, we identified 3 phosphorylation sites in Vts1 (Figure 6C). However, only S175 and S420 are differentially phosphorylated in the presence of Pmk1 in our PRM analysis (Figure 6D). To differentiate between direct and indirect effects of the absence of Pmk1 activity, we used a Pmk1 analog-sensitive mutant ($pmk1^{AS}$),⁶ which can be inhibited selectively by addition of the ATP analog 1-Naphthyl-PP1 (1Na-PP1). In this way, we were able to inhibit Pmk1 *in vivo* during early appressorium formation (Figure 6E). We used PRM to accurately measure phosphopeptide abundance, which showed that specific inhibition of Pmk1 at 1–4 h post germination affects phosphorylation at S175 and S420 of Vts1, but not at T14 (Figures 6D and 6E). To test whether Pmk1 phosphorylates Vts1 at S175 and S420, we carried out an *in vitro* kinase assay using recombinant Vts1 and Pmk1. We used a recombinant constitutively active MAPKK from tobacco (*Nicotiana tabacum*) NtMEK2^{DD} to activate Pmk1, as previously shown^{7,51} (Figure S5). The *in vitro* kinase assay showed that Pmk1 specifically phosphorylates Vts1 in a [S/T]P motif (Figures 6B and S6D), and MS demonstrated that S175 and S420 are indeed phosphorylated by Pmk1 (Figure S5E). These results indicate that Pmk1 can associate with and specifically phosphorylate Vts1 at residues S175 and S420, consistent with Vts1 being a direct substrate of Pmk1.

To investigate the role of Vts1 in fungal pathogenicity, we generated a targeted deletion mutant of *VTS1* in *M. oryzae* Guy11 (Figure S6). We observed that 58% of $\Delta vts1$ appressoria show aberrant development compared with Guy11 (Figures 6F

Figure 5. Quantitative phosphoproteomics defines 32 putative targets of the Pmk1 MAPK pathway

(A) Schematic representation of the phosphoproteomic workflow for the quantitative analysis experiment between Guy11 and $\Delta pmk1$ to determine putative Pmk1 targets in *M. oryzae*. Spores and germinated cells were synchronized at 0, 1, 1.5, 2, 4, and 6 h. Phosphopeptides were enriched using TiO₂ microspheres and were subjected to liquid chromatography-tandem mass spectrometry (LC-MS/MS). Samples for 3 biological replicates were analyzed by parallel reaction monitoring (PRM).

(B) Heatmap to show the differentially phosphorylated phosphopeptides in Guy11 and $\Delta pmk1$. Each row corresponds to a single phosphopeptide measured in 3 biological replicates. See also Figure S4.

(C) Schematic representation of components of the Pmk1 signaling pathway in *M. oryzae*. Differentially phosphorylated residues are indicated for each protein (adjusted $p \leq 0.05$).

(D) Bar graphs to show relative normalized intensity determined by PRM of peptides associated to Mst11, Mst7, Pmk1, Mst50, and Hox7 during early infection from 0 to 6 h in Guy11 and $\Delta pmk1$.

(E) Yeast-two-hybrid (Y2H) assay to determine the interaction of Pmk1 with its putative direct targets. Protein interactions were tested in yeast grown on SD medium –Trp –Leu –Ade –His + alpha X-gal + Au (4DO panels). Viability of all transformed yeast cells was demonstrated by growth on SD medium –Trp –Leu (2DO panels). Yeast cells were inoculated onto media as a 10-fold dilution series. Mst12 was used as the positive control.

Table 1. Pmk1 putative targets identified during appressorium formation by PRM

Gene ID	Name	Function/process	Pmk1-dependent phosphorylation site	<i>M. oryzae</i> null mutant phenotype	Reference
MGG_01311	nuclear elongation protein	uncharacterized	S216	–	–
MGG_03218	calciressin protein	uncharacterized	T190, S193	–	–
MGG_03558	PH domain protein	uncharacterized	S666, S688, S875	–	–
MGG_05220	S/T protein kinase	uncharacterized	S267, S274, S320	–	–
MGG_06334	Vts1	uncharacterized	S175, S420	appressorium formation, virulence	this study
MGG_06403	PH domain protein	uncharacterized	S272, S275	–	–
MGG_07714	actin cytoskeleton organization protein	uncharacterized	S258	–	–
MGG_09293	cell division control protein	uncharacterized	S97, S125, Y129, S133	–	–
MGG_09554	anaphase-promoting complex subunit	uncharacterized	S295	–	–
MGG_09697	PH domain protein	uncharacterized	T798, T899	–	–
MGG_10538	RSC complex subunit	uncharacterized	T512	appressorium formation	Jeon et al. ²⁵
MGG_00345	RIM15	kinases	S402, S625, S633	virulence	Jeon et al. ²⁵ ; Motoyama et al. ³⁸
MGG_00803	SNF1	kinases	S90	conidiation, virulence	Yi et al. ³⁹ ; Zeng et al. ⁴⁰
MGG_01279	KIN1	kinases	S914, T918, S920	growth, virulence	Luo et al. ⁴¹
MGG_04790	CDS1	kinases	S1174	overcomes hydroxyurea-induced arrest of appressorium	Osés-Ruiz et al. ⁴²
MGG_08097	YCK1	kinases	S359	growth, conidiation, virulence	Shi et al. ⁴³
MGG_06393	Atg1	autophagy	S476, S547	virulence	Kershaw and Talbot ³⁶
MGG_00454	Atg13	autophagy	S517, S519, S920	virulence	Kershaw and Talbot ³⁶
MGG_07667	Atg17	autophagy	S207, S209, S211, S214	virulence	Kershaw and Talbot ³⁶
MGG_03139	Atg18	autophagy	S287, S295	virulence	Kershaw and Talbot ³⁶
MGG_08061	Atg28	autophagy	S399	none	Kershaw and Talbot ³⁶
MGG_14847	Mst11	Pmk1 pathway	T551, S557	virulence	Zhao et al. ¹⁰
MGG_00800	Mst7	Pmk1 pathway	S351, S358, S370	virulence	Zhao et al. ¹⁰
MGG_05199	Mst50	Pmk1 pathway	S260	virulence	Park et al. ¹¹
MGG_01836	FAR1	transcription factor	S41	lipid metabolism	bin Yusof et al. ⁴⁴
MGG_06258	FKH1	transcription factor	S491, S641	germination, virulence	Park et al. ⁴⁵
MGG_12865	HOX7	transcription factor/Pmk1 pathway	S126, S158, T161, S163	appressorium formation, virulence	Osés-Ruiz et al. ⁷ ; Sweigard et al. ⁴⁶
MGG_04708	SOM1	transcription factor/cAMP pathway	S228, T588, T589, S591, S595	growth, conidiation, virulence	Yan et al. ⁴⁷
MGG_09898	MAC1 (XP_365053.1)	cAMP pathway	S75	growth, conidiation, virulence, sexual reproduction	Choi and Dean ⁴⁸

(Continued on next page)

Table 1. Continued

Gene ID	Name	Function/process	Pmk1-dependent phosphorylation site	<i>M. oryzae</i> null mutant phenotype	Reference
MGG_06726	Septin4	cytoskeleton related	S313, S314, S318	virulence	Dagdas et al. ²²
MGG_03196	RCM1	transcriptional regulator	S645	–	–
MGG_01376	PTP2	phosphatase	S288	virulence	Liu et al. ⁴⁹

and 6G), and $\Delta vts1$ mutants were severely impaired in their ability to cause rice blast disease (Figure S6). To study the role of Pmk1-dependent phosphorylation of Vts1, we generated phosphomimetic and non-phosphorylatable (“phosphodead”) alleles of *VTS1* and transformed these into the $\Delta vts1$ mutant. We observed that rice blast disease and infection progression are severely impaired in the strain complemented with the phosphodead allele *VTS1*^{A175}, but not by any of the other phosphorylation mutant variants (Figures 6H and 6I). This provides strong evidence that Pmk1-dependent phosphorylation of S175 of Vts1 is necessary for the development rice blast disease. Consistent with the requirement of S175 for fungal virulence, we found that Vts1 S175 is conserved among filamentous fungi, while S420 is not conserved in other fungal species (Figure S7). This suggests that S175 and S420 fulfill different, distinct functions. When considered together, these results demonstrate that quantitative phosphoproteomics has the capacity to identify completely novel regulators of fungal virulence and enable the functional characterization of signaling pathways that govern plant infection by pathogenic fungi.

DISCUSSION

Fungal pathogenicity is a complex phenotype that encompasses the ability of many fungal pathogens to develop specialized infection structures to breach the tough outer layers of plants, insects, or human cells, to colonize living host tissue, to suppress immunity by deployment of large families of effector proteins, and finally to kill host cells and produce new infective propagules to infect new hosts. Very few global regulators of fungal pathogenesis have been identified to date, but MAPKs appear to be widely conserved across fungi and in pathogenic species, and they have been shown to control invasive growth and virulence. The rice blast fungus is one of the most devastating pathogens in the world, and the MAPK Pmk1 is a master regulator of infection-related development, regulating appressorium morphogenesis,⁵ appressorium function^{7,36,52} and invasive growth in plant tissue.⁶ This single kinase has been shown to control 49% of total gene expression during appressorium development, suggesting a very broad role in the control of fungal development and physiology.⁷ Identifying the exact targets of master-regulator kinases across pathogenic fungi and understanding the degree of conservation between them could provide new information that can be exploited to control of some of the most devastating diseases across the world.

In this study, we aimed to test whether quantitative phosphoproteomics could provide insight into the biology of infection by pathogenic fungi and identify downstream processes via its

direct phosphorylation substrates. The first major conclusion of this study is that the phosphorylation landscape of fungal infection by the rice blast fungus is complex and highly dynamic. Dramatic changes in phosphorylation occur as early as initial contact to an inductive surface and extend to appressorium differentiation. We found a total of 8,005 peptides corresponding to 2,062 proteins, which change in abundance and/or are differentially phosphorylated in just 6 h of development. The approach revealed that critical physiological processes previously reported to be essential for infection are highly dynamic and tightly regulated by phosphorylation. These processes include autophagy, which is essential for recycling the contents of the three-celled conidium into the unicellular appressorium²¹; lipid metabolism,^{52,53} which is essential for glycerol synthesis that acts as the compatible solute in an appressorium for generation of its enormous turgor; and melanization, which is essential for the appressorium to generate pressure.^{54,55} Many other processes, including cell cycle regulation, cell wall biogenesis, intracellular trafficking, and secondary metabolism, are also clearly regulated by dynamic changes in phosphorylation during infection.

The second major conclusion of the study is that patterns of phosphorylation have been conserved across diverse fungal species, revealing phosphorylation signatures correlated with fungal pathogenesis and infection structure development, many of which are likely to be dependent on Pmk1-related MAPK activity. Comparative analysis with 41 fungal species provided evidence that elements of the phosphorylation landscape identified in *M. oryzae* are conserved across different fungal species. A subset of phosphorylation sites are, for example, highly conserved in plant-associated fungal species, with further phosphosites conserved only in fungal pathogens that invade cereal hosts and others only present in fungal pathogens that elaborate melanized force-generating appressoria, like the blast fungus. These phosphosites have the potential to enable mining of conserved physiological processes associated with fungal pathogenesis, including infection structure development and the invasion of host tissue. Specific processes regulated by patterns of phosphorylation, for example, in *Colletotrichum* and *Magnaporthe*, include trehalose and glycogen metabolism, regulated lipolysis, cytoskeletal remodeling, and Bin-Amphiphysin-Rvs (BAR) domain proteins implicated in membrane curvature generation. These make sense in the context of development of a melanized, highly pressurized appressorium, but have not been studied in a comparative way between these species before.

Quantitative phosphoproteomic analysis enabled the detailed analysis of Pmk1-dependent phosphorylation in *M. oryzae*,

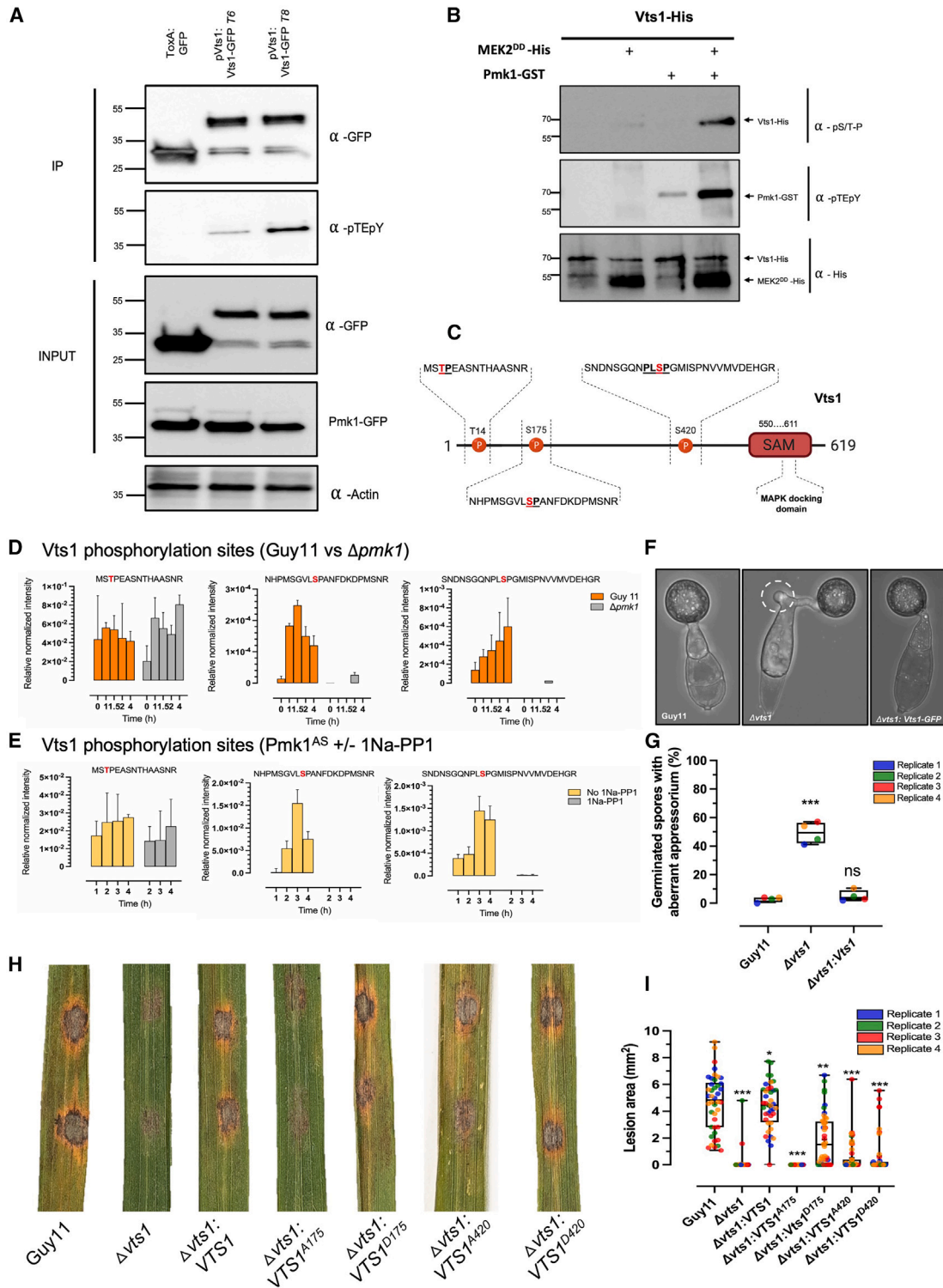


Figure 6. Vts1 is a novel target of the Pmk1 MAPK pathway necessary for rice blast disease

(A) Co-immunoprecipitation of Vts1-GFP. C-terminal GFP-tagged Vts1 was transformed into *M. oryzae* Guy11. Anti-pTEpY antiserum was used to detect double phosphorylated Pmk1. Immunoprecipitates obtained with anti-GFP antiserum and total proteins extracts were probed with appropriate antisera. Co-immunoprecipitation was repeated twice with similar results and Vts1-GFP bait protein identity was verified by LC-MS/MS.

(B) Western blot analysis of *in vitro* phosphorylation experiment between Pmk1 and Vts1 (N-terminally tagged with 6xHis). Proteins were immunoblotted with appropriate antisera (listed on the right). Arrows indicate expected band sizes. See also Figure S5.

(legend continued on next page)

revealing the specific signaling pathways targeted by the MAPK. These include the cAMP-dependent protein kinase A pathway, which serves a role both in surface sensing and the physiological regulation of compatible solute generation in the appressorium,^{1,2} and the regulators of autophagy, such as the Atg1 kinases, Atg13 and Atg17, which initiate phagophore formation at the onset of autophagy.⁵⁶ This link is consistent with previous studies in which autophagy was shown to be impaired in a $\Delta pmk1$ mutant,³⁶ but also shows the likely mechanism of by which Pmk1 exerts this control. Further insights have also been provided, however, such as the link with the Sln1 turgor sensor kinase, which is necessary to regulate polarized growth and penetration peg emergence once a threshold of turgor has been generated.^{3,4} Pmk1 is necessary for phosphorylation of the Sln1 histidine kinase and an interacting stretch-activated gated ion channel protein Mic1, as well as the components of the cell integrity pathway, such as protein kinase C, that are necessary for regulating the changes in cell wall structure associated with the resumption of polarized growth. Interestingly, the NADPH oxidase Nox2, which is necessary for septin aggregation at the appressorium pore, is also phosphorylated in a Pmk1-dependent manner, along with its Bem1 regulator. Similarly, the newly identified Vast1 pathway,⁵⁷ which is necessary for target of rapamycin (TOR)-dependent plasma membrane homeostasis, is also regulated in a Pmk1-dependent manner. This is also consistent with aminophospholipid regulators Pde1⁵⁸ and Apt2,²⁹ which are both necessary for appressorium function, being phosphorylated in a Pmk1-dependent manner. A third major conclusion of our study is therefore that quantitative phosphoproteomics can provide unparalleled insight into the regulatory processes controlled by Pmk1 during infection.

To test the ability to identify and characterize direct substrates of the Pmk1 MAPK, we focused on investigating a phosphorylated Pmk1 interactor called Vts1, a protein of unknown function in the rice blast fungus. We observed that Vts1 contains a sterile alpha motif (SAM) domain. SAM-domain-containing proteins have been previously reported as important regulators of MAPK signaling cascades,⁵⁹ and proteins containing SAM domains are versatile because this domain has been documented to take part in various interactions. They can, for example, show binding affinity to other SAM and non-SAM domain proteins, but can also show binding affinity to lipids and RNA.⁶⁰ Importantly, SAM domains have been reported to mediate associations of MAPK modules in different fungi. In *Schizosaccharomyces*

pombe, for instance, association between Ste4 and Byr2 occurs via a SAM motif.⁶¹ Similarly, in *S. cerevisiae*, the interaction between Ste11 and Ste50 is mediated by a SAM domain.⁶² In *M. oryzae*, the MAPKK Mst11 and the putative scaffold protein Mst50 in the Pmk1 pathway also both contain SAM domains.¹⁰ Furthermore, it has been demonstrated that Mst50-Mst11 interaction occurs via their respective SAM domains and that this is essential for appressorium development and plant infection.¹¹ In this study, we have provided evidence that Vts1 is phosphorylated directly by Pmk1 based on PRM, the analysis of a conditional analog-sensitive Pmk1 mutant, and an *in vitro* kinase assay. Furthermore, Vts1 is important for fungal virulence and necessary for correct appressorium morphogenesis. Vts1 has also been shown to be required for plant infection by *Fusarium oxysporum*.⁶³ Finally, we demonstrated that a single Vts1 phosphosite S175 is necessary for its biological activity during plant infection, and the serine at position 175 in *M. oryzae* is conserved in Vts1 in *Fusarium* species. These results therefore validate the use of phosphoproteomics as a means of identifying determinants of pathogenicity in the blast fungus and thereby revealing how Pmk1 exerts such a major role in the regulation of fungal infection.

When considered together, this study demonstrates the importance of phosphoproteomic changes during infection-related development by a pathogenic fungus. The conservation of nearly 1,200 phosphorylated residues in a group of 41 fungal species also reveals proteins required for core functions as well as potential phosphoproteins associated with a plant pathogenic lifestyle. This underscores the potential of our phosphoproteome datasets as a resource that can be mined by the fungal research community to identify novel virulence determinants in a wide range of fungal species.

Limitations of the study

Our study has quantified changes in the phosphoproteome during infection-related development, but due to the use of an artificial hydrophobic surface to induce appressorium formation, a subset of the phosphorylation events may be specific for these conditions. Using an artificial hydrophobic surface, however, allowed us to induce synchronized appressorium development and obtain deep phosphoproteomic coverage for *M. oryzae*. This approach was necessary because it enabled the comprehensive profiling of fungal proteins without interference from plant proteins, which would otherwise have dominated the detected phosphopeptides. Appressorium development is

(C) Schematic diagram to show Vts1 phosphorylated residues T14, S175, and S420, and position of the predicted SAM domain.

(D and E) Relative normalized intensity determined by PRM of Vts1 phosphopeptides associated with T14, S175, and S420 during appressorium development from 0 to 4 h in *M. oryzae* for (D) Guy11 and the $\Delta pmk1$ mutant, and (E) the analog-sensitive mutant $pmk1^{AS}$, in the presence or absence of the inhibitor 1Na-PP1. Data in (D) and (E) represent the average for 3 biological replicate measurements. Error bars represent standard deviation.

(F) Micrographs to show appressorium development of Guy11, $\Delta vts1$, and $\Delta vts1:VTS1$ -GFP strains. Conidia were harvested from Guy11 and $\Delta vts1$ mutants, inoculated onto glass coverslips, and observed at 24 h. Scale bars, 10 μ m. See also Figure S6.

(G) Bar chart showing the frequency of conidial germination from one and two cells. 3 biological replicates were carried out with 100 appressoria recorded per replicate. * $p < 0.05$; ** $p < 0.01$; *** $p < 0.001$ represent significant differences, using an unpaired two-tailed Student's t test. Data are from 4 biological replicates. Error bars represent standard deviation.

(H) Leaf drop assay using 3-week-old seedlings of rice cultivar CO-39 that were inoculated with equal amounts of conidial suspensions of Guy11, $\Delta vts1$, and Vts1 phosphorylation mutant strains (10^5 conidia mL^{-1}) in 0.2% gelatin. Seedlings were incubated for 5 days to develop blast disease at 26°C. Fully susceptible, sporulating disease lesions can be distinguished by their gray centers.

(I) Bar chart to show the lesion size for each *M. oryzae* phosphoallele. * $p < 0.05$; ** $p < 0.01$; *** $p < 0.001$ represent significance using unpaired two-tailed Student's t test. Data from 4 biological replicates. Error bars represent standard deviation.

well-documented to occur on artificial substrates and has been used to define transcriptional networks associated with plant infection⁷ and key developmental processes such as septin ring formation, which are essential for rice blast disease.^{4,22}

STAR★METHODS

Detailed methods are provided in the online version of this paper and include the following:

- **KEY RESOURCES TABLE**
- **RESOURCE AVAILABILITY**
 - Lead contact
 - Materials availability
 - Data and code availability
- **EXPERIMENTAL MODEL AND STUDY PARTICIPANT DETAILS**
 - *Magnaporthe oryzae* and growth conditions
 - *Oryza sativa* and growth conditions
- **METHOD DETAILS**
 - *In vitro* appressorium assay
 - Protein extraction and phosphopeptide enrichment
 - Mass-Spectrometry analysis
 - Plasmid construction
 - DNA purification
 - Southern blotting
 - Whole genome sequencing
 - Protoplast-mediated transformation of *M. oryzae*
 - RNA extraction and cDNA synthesis
 - Virulence analysis
 - Light microscopy
 - Cryo-scanning electron microscopy
 - Yeast-two-hybrid (Y2H) analysis
 - Recombinant proteins production and purification
 - Protein extraction and Co-immunoprecipitation (Co-IP) assay
 - *In vitro* phosphorylation assay
 - Generation of schematics
- **QUANTIFICATION AND STATISTICAL ANALYSIS**
 - Functional categorization of Pmk1 targets
 - Spectral library generation and raw data processing
 - Label free quantification at MS1 level
 - Phosphosite conservation analysis
 - Clustering of phosphosites by conservation
 - Clustering and GO analysis
 - Parallel Reaction Monitoring (PRM)
 - Differential phosphosite analysis

SUPPLEMENTAL INFORMATION

Supplemental information can be found online at <https://doi.org/10.1016/j.cell.2024.04.007>.

ACKNOWLEDGMENTS

We thank Prof. Sophien Kamoun for critical input on this manuscript. We thank Phil Robinson at the John Innes Centre (JIC) for providing technical support on photography. We thank Dr. Iris Eisermann for providing the Septin4 pGBK7 construct. This work was supported by grants to N.J.T. from the Gatsby Charitable Foundation and Biotechnology and Biological Sciences Research Council (BBSRC) BBS/E/J/000PR9797, a BBSRC grant to N.J.T. and F.L.H.M. (BB/V016342/1), and the BBSRC core capability grant to Bioimaging facilities at the JIC. N.C.-M. was supported by the John Innes Foundation, the Sainsbury Laboratory Rotation Programme PhD Studentship, and the Consejo Nacional de Humanidades, Ciencia y Tecnologías (CONAHCYT). M.O.-R. was supported by the Spanish Ministry of Science and Innovation Grant, PID2020-120188RJ-I00, financed by MICIN/AEI. M.O.R. is a recipient of the Ramon y Cajal grant RYC2021-032146-I, funded by MCIN/AEI/10.13039/

5011000110033, “European Union Next Generation EU/PRTR,” and the European Union (HORIZON-ERC2021-101076478).

AUTHOR CONTRIBUTIONS

N.J.T. and F.L.H.M. conceived the project. N.J.T. and F.L.H.M. guided the execution of the experiments and oversaw the project. N.C.M., M.O.-R., P.D., C.J., L.S.R., M.J.A.B., A.E., J.S., B.T., X.Y., W.M., K.C.F., V.W., D.M., and F.L.H.M. did the experiments and analyzed the data. N.C.-M. prepared figures and tables. N.C.-M., N.J.T., and F.L.H.M. wrote the manuscript, with contributions from all authors.

DECLARATION OF INTERESTS

The authors declare no competing interests.

Received: August 28, 2023

Revised: February 2, 2024

Accepted: April 10, 2024

Published: May 9, 2024

REFERENCES

1. Cruz-Mireles, N., Eseola, A.B., Osés-Ruiz, M., Ryder, L.S., and Talbot, N.J. (2021). From appressorium to transpressorium—defining the morphogenetic basis of host cell invasion by the rice blast fungus. *PLoS Pathog.* *17*, e1009779. <https://doi.org/10.1371/JOURNAL.PPAT.1009779>.
2. Ryder, L.S., Cruz-Mireles, N., Molinari, C., Eisermann, I., Eseola, A.B., and Talbot, N.J. (2022). The appressorium at a glance. *J. Cell Sci.* *135*, jcs259857. <https://doi.org/10.1242/jcs.259857>.
3. Ryder, L.S., Dagdas, Y.F., Kershaw, M.J., Venkataraman, C., Madzvamuse, A., Yan, X., Cruz-Mireles, N., Soanes, D.M., Osés-Ruiz, M., Styles, V., et al. (2019). A sensor kinase controls turgor-driven plant infection by the rice blast fungus. *Nature* *574*, 423–427. <https://doi.org/10.1038/s41586-019-1637-x>.
4. Ryder, L.S., Lopez, S.G., Michels, L., Eseola, A.B., Sprakel, J., Ma, W., and Talbot, N.J. (2023). A molecular mechanosensor for real-time visualization of appressorium membrane tension in *Magnaporthe oryzae*. *Nat. Microbiol.* *8*, 1508–1519. <https://doi.org/10.1038/s41564-023-01430-x>.
5. Xu, J.R., and Hamer, J.E. (1996). MAP kinase and cAMP signaling regulate infection structure formation and pathogenic growth in the rice blast fungus *Magnaporthe grisea*. *Genes Dev.* *10*, 2696–2706. <https://doi.org/10.1101/gad.10.21.2696>.
6. Sakulkoo, W., Osés-Ruiz, M., Oliveira Garcia, E., Soanes, D.M., Littlejohn, G.R., Hacker, C., Correia, A., Valent, B., and Talbot, N.J. (2018). A single fungal MAP kinase controls plant cell-to-cell invasion by the rice blast fungus. *Science* *359*, 1399–1403. <https://doi.org/10.1126/science.aag0892>.
7. Osés-Ruiz, M., Cruz-Mireles, N., Martin-Urdiroz, M., Soanes, D.M., Eseola, A.B., Tang, B., Derbyshire, P., Nielsen, M., Cheema, J., Were, V., et al. (2021). Appressorium-mediated plant infection by *Magnaporthe oryzae* is regulated by a Pmk1-dependent hierarchical transcriptional network. *Nat. Microbiol.* *6*, 1383–1397. <https://doi.org/10.1038/S41564-021-00978-W>.
8. Elion, E.A., Grisafi, P.L., and Fink, G.R. (1990). FUS3 encodes a cdc2+/CDC28-related kinase required for the transition from mitosis into conjugation. *Cell* *60*, 649–664. [https://doi.org/10.1016/0092-8674\(90\)90668-5](https://doi.org/10.1016/0092-8674(90)90668-5).
9. Elion, E.A., Brill, J.A., and Fink, G.R. (1991). FUS3 represses CLN1 and CLN2 and in concert with KSS1 promotes signal transduction. *Proc. Natl. Acad. Sci. USA* *88*, 9392–9396. <https://doi.org/10.1073/PNAS.88.21.9392>.
10. Zhao, X., Kim, Y., Park, G., and Xu, J.-R. (2005). A mitogen-activated protein kinase cascade regulating infection-related morphogenesis in *Magnaporthe grisea*. *Plant Cell* *17*, 1317–1329. <https://doi.org/10.1105/tpc.104.029116>.

11. Park, G., Xue, C., Zhao, X., Kim, Y., Orbach, M., and Xu, J.-R. (2006). Multiple upstream signals converge on the adaptor protein Mst50 in *Magnaporthe grisea*. *Plant Cell* *18*, 2822–2835. <https://doi.org/10.1105/tpc.105.038422>.
12. Li, G., Zhou, X., Kong, L., Wang, Y., Zhang, H., Zhu, H., Mitchell, T.K., Dean, R.A., and Xu, J.-R. (2011). MoSfl1 is important for virulence and heat tolerance in *Magnaporthe oryzae*. *PLoS One* *6*, e19951. <https://doi.org/10.1371/journal.pone.0019951>.
13. Zhang, H., Xue, C., Kong, L., Li, G., and Xu, J.-R. (2011). A Pmk1-interacting gene is involved in appressorium differentiation and plant infection in *Magnaporthe oryzae*. *Eukaryot. Cell* *10*, 1062–1070. <https://doi.org/10.1128/EC.00007-11>.
14. Rispaill, N., Soanes, D.M., Ant, C., Czajkowski, R., Grünler, A., Huguet, R., Perez-Nadales, E., Poli, A., Sartorel, E., Valiante, V., et al. (2009). Comparative genomics of MAP kinase and calcium-calmodulin signalling components in plant and human pathogenic fungi. *Fungal Genet. Biol.* *46*, 287–298. <https://doi.org/10.1016/J.FGB.2009.01.002>.
15. Jiang, C., Zhang, X., Liu, H., and Xu, J.-R. (2018). Mitogen-activated protein kinase signaling in plant pathogenic fungi. *PLoS Pathog.* *14*, e1006875. <https://doi.org/10.1371/journal.ppat.1006875>.
16. Savary, S., Willcoquet, L., Pethybridge, S.J., Esker, P., McRoberts, N., and Nelson, A. (2019). The global burden of pathogens and pests on major food crops. *Nat. Ecol. Evol.* *3*, 430–439. <https://doi.org/10.1038/s41559-018-0793-y>.
17. Strumillo, M.J., Oplová, M., Viéitez, C., Ochoa, D., Shahraz, M., Busby, B.P., Sopko, R., Studer, R.A., Perrimon, N., Panse, V.G., et al. (2019). Conserved phosphorylation hotspots in eukaryotic protein domain families. *Nat. Commun.* *10*, 1–11. <https://doi.org/10.1038/s41467-019-09952-x>.
18. Takác, T., and Šamaj, J. (2015). Advantages and limitations of shot-gun proteomic analyses on Arabidopsis plants with altered MAPK signaling. *Front. Plant Sci.* *6*, 107. <https://doi.org/10.3389/FPLS.2015.00107/BIBTEX>.
19. Savage, S.R., and Zhang, B. (2020). Using phosphoproteomics data to understand cellular signaling: A comprehensive guide to bioinformatics resources. *Clin. Proteomics* *17*, 1–18. <https://doi.org/10.1186/S12014-020-09290-X/TABLES/7>.
20. Zhang, X., Bian, Z., and Xu, J.R. (2018). Assays for MAP kinase activation in *Magnaporthe oryzae* and other plant pathogenic fungi. *Methods Mol. Biol.* *1848*, 93–101. https://doi.org/10.1007/978-1-4939-8724-5_8.
21. Veneault-Fourrey, C., Barooah, M., Egan, M., Wakley, G., and Talbot, N.J. (2006). Autophagic fungal cell death is necessary for infection by the rice blast fungus. *Science* *312*, 580–583. <https://doi.org/10.1126/science.1124550>.
22. Dagdas, Y.F., Yoshino, K., Dagdas, G., Ryder, L.S., Bielska, E., Steinberg, G., and Talbot, N.J. (2012). Septin-mediated plant cell invasion by the rice blast fungus, *Magnaporthe oryzae*. *Science* *336*, 1590–1595. <https://doi.org/10.1126/science.1222934>.
23. Dulal, N., Rogers, A., Wang, Y., and Egan, M. (2020). Dynamic assembly of a higher-order septin structure during appressorium morphogenesis by the rice blast fungus. *Fungal Genet. Biol.* *140*, 103385. <https://doi.org/10.1016/J.FGB.2020.103385>.
24. Li, G., Gong, Z., Dulal, N., Marroquin-Guzman, M., Rocha, R.O., Richter, M., and Wilson, R.A. (2023). A protein kinase coordinates cycles of autophagy and glutaminolysis in invasive hyphae of the fungus *Magnaporthe oryzae* within rice cells. *Nat. Commun.* *14*, 4146. <https://doi.org/10.1038/s41467-023-39880-w>.
25. Jeon, J., Park, S.-Y., Chi, M.-H., Choi, J., Park, J., Rho, H.-S., Kim, S., Goh, J., Yoo, S., Choi, J., et al. (2007). Genome-wide functional analysis of pathogenicity genes in the rice blast fungus. *Nat. Genet.* *39*, 561–565. <https://doi.org/10.1038/ng2002>.
26. Mir, A.A., Park, S.-Y., Sadat, M.A., Kim, S., Choi, J., Jeon, J., and Lee, Y.-H. (2015). Systematic characterization of the peroxidase gene family provides new insights into fungal pathogenicity in *Magnaporthe oryzae*. *Sci. Rep.* *5*, 11831. <https://doi.org/10.1038/srep11831>.
27. Han, J.H., Lee, H.M., Shin, J.H., Lee, Y.H., and Kim, K.S. (2015). Role of the MoYAK1 protein kinase gene in *Magnaporthe oryzae* development and pathogenicity. *Environ. Microbiol.* *17*, 4672–4689. <https://doi.org/10.1111/1462-2920.13010>.
28. Tanaka, S., Yamada, K., Yabumoto, K., Fujii, S., Huser, A., Tsuji, G., Koga, H., Dohi, K., Mori, M., Shiraishi, T., et al. (2007). *Saccharomyces cerevisiae* SSD1 orthologues are essential for host infection by the ascomycete plant pathogens *Colletotrichum lagenarium* and *Magnaporthe grisea*. *Mol. Microbiol.* *64*, 1332–1349. <https://doi.org/10.1111/J.1365-2958.2007.05742.X>.
29. Gilbert, M.J., Thornton, C.R., Wakley, G.E., and Talbot, N.J. (2006). A P-type ATPase required for rice blast disease and induction of host resistance. *Nature* *440*, 535–539. <https://doi.org/10.1038/nature04567>.
30. Beltrao, P., Albanèse, V., Kenner, L.R., Swaney, D.L., Burlingame, A., Villén, J., Lim, W.A., Fraser, J.S., Frydman, J., and Krogan, N.J. (2012). Systematic functional prioritization of protein posttranslational modifications. *Cell* *150*, 413–425. <https://doi.org/10.1016/j.cell.2012.05.036>.
31. Studer, R.A., Rodriguez-Mias, R.A., Haas, K.M., Hsu, J.I., Viéitez, C., Solé, C., Swaney, D.L., Stanford, L.B., Liachko, I., Böttcher, R., et al. (2016). Evolution of protein phosphorylation across 18 fungal species. *Science* *354*, 229–232. <https://doi.org/10.1126/science.aaf2144>.
32. Zhao, X., and Xu, J.-R. (2007). A highly conserved MAPK-docking site in Mst7 is essential for Pmk1 activation in *Magnaporthe grisea*. *Mol. Microbiol.* *63*, 881–894. <https://doi.org/10.1111/j.1365-2958.2006.05548.x>.
33. Li, G., Zhang, X., Tian, H., Choi, Y.-E., Tao, W.A., and Xu, J.-R. (2017). MST50 is involved in multiple MAP kinase signaling pathways in *Magnaporthe oryzae*. *Environ. Microbiol.* *19*, 1959–1974. <https://doi.org/10.1111/1462-2920.13710>.
34. Yue, X., Que, Y., Xu, L., Deng, S., Peng, Y., Talbot, N.J., and Wang, Z. (2016). ZNF1 encodes a putative C2H2 zinc-finger protein essential for appressorium differentiation by the rice blast fungus *Magnaporthe oryzae*. *Mol. Plant Microbe Interact.* *29*, 22–35. <https://doi.org/10.1094/MPMI-09-15-0201-R>.
35. Cao, H., Huang, P., Zhang, L., Shi, Y., Sun, D., Yan, Y., Liu, X., Dong, B., Chen, G., Snyder, J.H., et al. (2016). Characterization of 47 Cys2-His2 zinc finger proteins required for the development and pathogenicity of the rice blast fungus *Magnaporthe oryzae*. *New Phytol.* *211*, 1035–1051. <https://doi.org/10.1111/NPH.13948>.
36. Kershaw, M.J., and Talbot, N.J. (2009). Genome-wide functional analysis reveals that infection-associated fungal autophagy is necessary for rice blast disease. *Proc. Natl. Acad. Sci. USA* *106*, 15967–15972. <https://doi.org/10.1073/PNAS.0901477106>.
37. Foster, A.J., Were, V.M., Yan, X., Win, J., Harant, A., Langner, T., Kamoun, S., and Talbot, N.J. (2021). MagnaGenes (v.1.0): an open science database of gene function studies in the blast fungus *Magnaporthe oryzae*. <https://doi.org/10.5281/ZENODO.4647766>.
38. Motoyama, T., Ochiai, N., Morita, M., Iida, Y., Usami, R., and Kudo, T. (2008). Involvement of putative response regulator genes of the rice blast fungus *Magnaporthe oryzae* in osmotic stress response, fungicide action, and pathogenicity. *Curr. Genet.* *54*, 185–195. <https://doi.org/10.1007/s00294-008-0211-0>.
39. Yi, M., Park, J.H., Ahn, J.H., and Lee, Y.H. (2008). MoSNF1 regulates sporulation and pathogenicity in the rice blast fungus *Magnaporthe oryzae*. *Fungal Genet. Biol.* *45*, 1172–1181. <https://doi.org/10.1016/J.FGB.2008.05.003>.
40. Zeng, X.Q., Chen, G.Q., Liu, X.H., Dong, B., Shi, H., Lu, J., and Lin, F. (2014). Crosstalk between SNF1 pathway and the peroxisome-mediated lipid metabolism in *Magnaporthe oryzae*. *PLoS One* *9*, e103124. <https://doi.org/10.1371/JOURNAL.PONE.0103124>.
41. Luo, Y., Zhang, H., Qi, L., Zhang, S., Zhou, X., Zhang, Y., and Xu, J.R. (2014). FgKin1 kinase localizes to the septal pore and plays a role in hyphal

- growth, ascospore germination, pathogenesis, and localization of Tub1 beta-tubulins in *Fusarium graminearum*. *New Phytol.* 204, 943–954. <https://doi.org/10.1111/NPH.12953>.
42. Osés-Ruiz, M., Sakulkoo, W., Littlejohn, G.R., Martin-Urdiroz, M., and Talbot, N.J. (2017). Two independent S-phase checkpoints regulate appressorium-mediated plant infection by the rice blast fungus *Magnaporthe oryzae*. *Proc. Natl. Acad. Sci. USA* 114, E237–E244. <https://doi.org/10.1073/pnas.1611307114>.
 43. Shi, H.B., Chen, N., Zhu, X.M., Su, Z.Z., Wang, J.Y., Lu, J.P., Liu, X.H., and Lin, F.C. (2019). The casein kinase MoYck1 regulates development, auto-phagy, and virulence in the rice blast fungus. *Virulence* 10, 719. <https://doi.org/10.1080/21505594.2019.1649588>.
 44. bin Yusof, M.T., Kershaw, M.J., Soanes, D.M., and Talbot, N.J. (2014). FAR1 and FAR2 regulate the expression of genes associated with lipid metabolism in the rice blast fungus *Magnaporthe oryzae*. *PLoS One* 9, e99760. <https://doi.org/10.1371/JOURNAL.PONE.0099760>.
 45. Park, J., Kong, S., Kim, S., Kang, S., and Lee, Y.H. (2014). Roles of Fork-head-box transcription factors in controlling development, pathogenicity, and stress response in *Magnaporthe oryzae*. *Plant Pathol. J.* 30, 136–150. <https://doi.org/10.5423/PPJ.OA.02.2014.0018>.
 46. Sweigard, J.A., Carroll, A.M., Farrall, L., Chumley, F.G., and Valent, B. (1998). *Magnaporthe grisea* pathogenicity genes obtained through insertional mutagenesis. *MPMI* 11, 404–412. <https://doi.org/10.1094/MPMI.1998.11.5.404>.
 47. Yan, X., Li, Y., Yue, X., Wang, C., Que, Y., Kong, D., Ma, Z., Talbot, N.J., and Wang, Z. (2011). Two novel transcriptional regulators are essential for infection-related morphogenesis and pathogenicity of the rice blast fungus *Magnaporthe oryzae*. *PLoS Pathog.* 7, e1002385. <https://doi.org/10.1371/JOURNAL.PPAT.1002385>.
 48. Choi, W., and Dean, R.A. (1997). The adenylate cyclase gene MAC1 of *Magnaporthe grisea* controls appressorium formation and other aspects of growth and development. *Plant Cell* 9, 1973–1983. <https://doi.org/10.1105/TPC.9.11.1973>.
 49. Liu, X., Zhou, Q., Guo, Z., Liu, P., Shen, L., Chai, N., Qian, B., Cai, Y., Wang, W., Yin, Z., et al. (2020). A self-balancing circuit centered on moosm1 kinase governs adaptive responses to host-derived ros in *Magnaporthe oryzae*. *eLife* 9, 1–28. <https://doi.org/10.7554/eLife.61605>.
 50. Yue, X., Que, Y., Deng, S., Xu, L., Osés-Ruiz, M., Talbot, N.J., Peng, Y., and Wang, Z. (2017). The cyclin dependent kinase subunit Cks1 is required for infection-associated development of the rice blast fungus *Magnaporthe oryzae*. *Environ. Microbiol.* 19, 3959–3981. <https://doi.org/10.1111/1462-2920.13796>.
 51. Mithoe, S.C., Ludwig, C., Pel, M.J., Cucinotta, M., Casartelli, A., Mbengue, M., Sklenar, J., Derbyshire, P., Robatzek, S., Pieterse, C.M., et al. (2016). Attenuation of pattern recognition receptor signaling is mediated by a MAP kinase kinase kinase. *EMBO Rep.* 17, 441–454. <https://doi.org/10.15252/embr.201540806>.
 52. Thines, E., Weber, R.W.S., and Talbot, N.J. (2000). MAP kinase and protein kinase A-dependent mobilization of triacylglycerol and glycogen during appressorium turgor generation by *Magnaporthe grisea*. *Plant Cell* 12, 1703–1718. <https://doi.org/10.1105/tpc.12.9.1703>.
 53. Wang, Z.Y., Soanes, D.M., Kershaw, M.J., and Talbot, N.J. (2007). Functional analysis of lipid metabolism in *Magnaporthe grisea* reveals a requirement for peroxisomal fatty acid β -oxidation during appressorium-mediated plant infection. *MPMI* 20, 475–491. <https://doi.org/10.1094/MPMI-20-5-0475>.
 54. de Jong, J.C., McCormack, B.J., Smirnov, N., and Talbot, N.J. (1997). Glycerol generates turgor in rice blast. *Nature* 389, 244. <https://doi.org/10.1038/38418>.
 55. Howard, R.J., and Valent, B. (1996). Breaking and entering: Host Penetration by the Fungal Rice Blast Pathogen *Magnaporthe grisea*. *Annu. Rev. Microbiol.* 50, 491–512. <https://doi.org/10.1146/annurev.micro.50.1.491>.
 56. Yamamoto, H., Fujioka, Y., Suzuki, S.W., Noshiro, D., Suzuki, H., Kondo-Kakuta, C., Kimura, Y., Hirano, H., Ando, T., Noda, N.N., et al. (2016). The intrinsically disordered protein Atg13 mediates supramolecular assembly of autophagy initiation complexes. *Dev. Cell* 38, 86–99. <https://doi.org/10.1016/J.DEVCEL.2016.06.015>.
 57. Zhu, X.M., Li, L., Cai, Y.Y., Wu, X.Y., Shi, H., Bin, L.S., Qu, Y.M., Naqvi, N.I., Del Poeta, M., et al. (2021). A VAST-domain protein regulates autophagy, membrane tension, and sterol homeostasis in rice blast fungus. *Autophagy* 17, 2939–2961. https://doi.org/10.1080/15548627.2020.1848129/SUPPL_FILE/KAUP_A_1848129_SM0951.ZIP.
 58. Balhadère, P.V., Foster, A.J., and Talbot, N.J. (1999). Identification of pathogenicity mutants of the rice blast fungus *Magnaporthe grisea* by insertional mutagenesis. *MPMI* 12, 129–142. <https://doi.org/10.1094/MPMI.1999.12.2.129>.
 59. Kim, C.A., and Bowie, J.U. (2003). SAM domains: uniform structure, diversity of function. *Trends Biochem. Sci.* 28, 625–628. <https://doi.org/10.1016/J.TIBS.2003.11.001>.
 60. Knight, M.J., Leettola, C., Gingery, M., Li, H., and Bowie, J.U. (2011). A human sterile alpha motif domain polymerizome. *Protein Sci.* 20, 1697–1706. <https://doi.org/10.1002/PRO.703>.
 61. Ramachander, R., Kim, C.A., Phillips, M.L., Mackereth, C.D., Thanos, C.D., McIntosh, L.P., and Bowie, J.U. (2002). Oligomerization-dependent association of the SAM domains from *Schizosaccharomyces pombe* Byr2 and Ste4. *J. Biol. Chem.* 277, 39585–39593. <https://doi.org/10.1074/jbc.M207273200>.
 62. Grimshaw, S.J., Mott, H.R., Stott, K.M., Nielsen, P.R., Evetts, K.A., Hopkins, L.J., Nietlispach, D., and Owen, D. (2004). Structure of the Sterile α Motif (SAM) domain of the *Saccharomyces cerevisiae* mitogen-activated protein kinase pathway-modulating protein STE50 and analysis of its interaction with the STE11 SAM. *J. Biol. Chem.* 279, 2192–2201. <https://doi.org/10.1074/jbc.M305605200>.
 63. Iida, Y., Fujiwara, K., Yoshioka, Y., and Tsuge, T. (2014). Mutation of FVS1, encoding a protein with a sterile alpha motif domain, affects asexual reproduction in the fungal plant pathogen *Fusarium oxysporum*. *FEMS Microbiol. Lett.* 351, 104–112. <https://doi.org/10.1111/1574-6968.12356>.
 64. Perez-Riverol, Y., Csordas, A., Bai, J., Bernal-Llinares, M., Hewapathirana, S., Kundu, D.J., Inuganti, A., Griss, J., Mayer, G., Eisenacher, M., et al. (2019). The PRIDE database and related tools and resources in 2019: improving support for quantification data. *Nucleic Acids Res.* 47, D442–D450. <https://doi.org/10.1093/NAR/GKY1106>.
 65. Sharma, V., Eckels, J., Taylor, G.K., Shulman, N.J., Stergachis, A.B., Joyner, S.A., Yan, P., Whiteaker, J.R., Halusa, G.N., Schilling, B., et al. (2014). Panorama: A targeted proteomics knowledge base. *J. Proteome Res.* 13, 4205–4210. <https://doi.org/10.1021/pr5006636>.
 66. Leung, H., Borromeo, E.S., Bernardo, M.A., and Nottogheh, J.L. (1988). Genetic analysis of virulence in the rice blast fungus *Magnaporthe grisea*. *Phytopathology* 78, 1227. <https://doi.org/10.1094/Phyto-78-1227>.
 67. Talbot, N.J., Ebbole, D.J., Hamer, J.E., Coughlan, S., and Valent, B. (1993). Identification and characterization of MPG1, a gene involved in pathogenicity from the rice blast fungus *Magnaporthe grisea*. *Plant Cell* 5, 1575–1590. <https://doi.org/10.1105/tpc.5.11.1575>.
 68. Molinari, C., and Talbot, N.J. (2022). A basic guide to the growth and manipulation of the blast fungus, *Magnaporthe oryzae*. *Curr. Protoc.* 2, e523. <https://doi.org/10.1002/CPZ1.523>.
 69. Mithoe, S.C., and Menke, F.L.H. (2023). Titanium oxide-based phosphopeptide enrichment from Arabidopsis seedlings. *Methods Mol. Biol.* 2581, 255–265. https://doi.org/10.1007/978-1-0716-2784-6_18.
 70. Valent, B., Farrall, L., and Chumley, F.G. (1991). *Magnaporthe grisea* genes for pathogenicity and virulence identified through a series of backcrosses. *Genetics* 127, 87–101. <https://doi.org/10.1093/GENETICS/127.1.87>.
 71. Menke, F.L.H., Kang, H.-G., Chen, Z., Park, J.M., Kumar, D., and Klessig, D.F. (2005). Tobacco transcription factor WRKY1 is phosphorylated by the

- MAP kinase SIPK and mediates HR-like cell death in tobacco. *MPMI* 18, 1027–1034. <https://doi.org/10.1094/MPMI-18-1027>.
72. Studier, F.W. (2005). Protein production by auto-induction in high-density shaking cultures. *Protein Expr. Purif.* 41, 207–234. <https://doi.org/10.1016/J.PEP.2005.01.016>.
 73. Conesa, A., and Götz, S. (2008). Blast2GO: A comprehensive suite for functional analysis in plant genomics. *Int. J. Plant Genomics* 2008, 1–12. <https://doi.org/10.1155/2008/619832>.
 74. Finn, R.D., Bateman, A., Clements, J., Coggill, P., Eberhardt, R.Y., Eddy, S.R., Heger, A., Hetherington, K., Holm, L., Mistry, J., et al. (2014). Pfam: the protein families database. *Nucleic Acids Res.* 42, D222–D230. <https://doi.org/10.1093/nar/gkt1223>.
 75. Li, H., Wang, J., Kuan, T.A., Tang, B., Feng, L., Wang, J., Cheng, Z., Sklenar, J., Derbyshire, P., Hulin, M., et al. (2023). Pathogen protein modularity enables elaborate mimicry of a host phosphatase. *Cell* 186, 3196–3207.e17. <https://doi.org/10.1016/J.CELL.2023.05.049>.
 76. Emms, D.M., and Kelly, S. (2019). OrthoFinder: phylogenetic orthology inference for comparative genomics. *Genome Biol.* 20, 238. <https://doi.org/10.1186/s13059-019-1832-y>.
 77. Buchfink, B., Reuter, K., and Drost, H.G. (2021). Sensitive protein alignments at tree-of-life scale using DIAMOND. *Nat. Methods* 18, 366–368. <https://doi.org/10.1038/s41592-021-01101-x>.
 78. Camacho, C., Coulouris, G., Avagyan, V., Ma, N., Papadopoulos, J., Bealer, K., and Madden, T.L. (2009). Blast+: architecture and applications. *BMC Bioinformatics* 10, 421. <https://doi.org/10.1186/1471-2105-10-421>.
 79. Developers factoextra: extract and visualize the results of multivariate data analyses. <https://rpkgs.datanovia.com/factoextra/index.html>.
 80. R Core Team (2021). R: A Language and Environment for Statistical Computing (R Foundation for Statistical Computing).
 81. Wickham, H., Averick, M., Bryan, J., Chang, W., McGowan, L., François, R., Grolemund, G., Hayes, A., Henry, L., Hester, J., et al. (2019). Welcome to the tidyverse. *J. Open Source Softw.* 4, 1686. <https://doi.org/10.21105/JOSS.01686>.
 82. Gu, Z., Eils, R., and Schlesner, M. (2016). Complex heatmaps reveal patterns and correlations in multidimensional genomic data. *Bioinformatics* 32, 2847–2849. <https://doi.org/10.1093/BIOINFORMATICS/BTW313>.
 83. Paradis, E., and Schliep, K. (2019). ape 5.0: an environment for modern phylogenetics and evolutionary analyses in R. *Bioinformatics* 35, 526–528. <https://doi.org/10.1093/BIOINFORMATICS/BTY633>.
 84. Galili, T. (2015). dendextend: an R package for visualizing, adjusting and comparing trees of hierarchical clustering. *Bioinformatics* 31, 3718–3720. <https://doi.org/10.1093/BIOINFORMATICS/BTV428>.
 85. Yu, G., Smith, D.K., Zhu, H., Guan, Y., and Lam, T.T.Y. (2017). ggtree: an R package for visualization and annotation of phylogenetic trees with their covariates and other associated data. *Methods Ecol. Evol.* 8, 28–36. <https://doi.org/10.1111/2041-210X.12628>.
 86. Wu, T., Hu, E., Xu, S., Chen, M., Guo, P., Dai, Z., Feng, T., Zhou, L., Tang, W., Zhan, L., et al. (2021). clusterProfiler 4.0: A universal enrichment tool for interpreting omics data. *Innov.* 2, 100141. <https://doi.org/10.1016/J.XINN.2021.100141>.
 87. Guo, H., Ahn, H.K., Sklenar, J., Huang, J., Ma, Y., Ding, P., Menke, F.L.H., and Jones, J.D.G. (2020). Phosphorylation-regulated activation of the Arabidopsis RRS1-R/RPS4 immune receptor complex reveals two distinct effector recognition mechanisms. *Cell Host Microbe* 27, 769–781.e6. <https://doi.org/10.1016/J.CHOM.2020.03.008>.
 88. MacLean, B., Tomazela, D.M., Shulman, N., Chambers, M., Finney, G.L., Frewen, B., Kern, R., Tabb, D.L., Liebler, D.C., and MacCoss, M.J. (2010). Skyline: an open source document editor for creating and analyzing targeted proteomics experiments. *Bioinformatics* 26, 966–968. <https://doi.org/10.1093/BIOINFORMATICS/BTQ054>.
 89. stamats – statistische Beratung – Prof. dr. rer. nat. Dipl. Math. (Univ.), Kohl, M. <https://www.stamats.de/>.

STAR★METHODS

KEY RESOURCES TABLE

REAGENT or RESOURCE	SOURCE	IDENTIFIER
Bacterial and virus strains		
<i>Escherichia coli</i> Stellar™ Chemically Competent Cell	Takara Bio	Cat# 636763
<i>Escherichia coli</i> DH5α	TIANGEN	Cat# CB101-02
<i>Escherichia coli</i> BL21 Rosetta (DE3)	Sigma-Aldrich	Cat# 70954
<i>Saccharomyces cerevisiae</i> Y2HGold	Takara Bio	Cat# 630498
Antibodies		
pTEpY (p44/42 MAPK) antibody	Cell Signaling Technology	Cat# 4370S; RRID: AB_2315112
pS/pT-P antibody	Abcam	Cat# ab9344; RRID: AB_307195
GFP antibody	Santa Cruz Biotechnology	Cat# sc-9996; RRID: AB_627695
Actin antibody	Agrisera com	Cat# AS13 2640; RRID: AB_2722610
6xHis antibody	Abcam	Cat# ab1187; RRID: AB_298652
Rabbit secondary antibody	Cell Signaling Technology	Cat# 7074S; RRID: AB_2099233
Chemicals, peptides, and recombinant proteins		
1, 16 Hexadecanediol	Sigma-Aldrich	Cat# 177482
Urea	Sigma-Aldrich	Cat# U5128
Protease Inhibitor Cocktail	Sigma-Aldrich	Cat# P9599
Tris (2-carboxyethyl) phosphine (TCEP)	Merck	Cat# 646547
Iodoacetamide	Merck	Cat# I6125
Ammonium bicarbonate	Merck	Cat# A6141
Trypsin	Pierce	Cat# 90058
Titanium dioxide (TiO ₂)	GL Science	Cat# 5020-75000
Phthalic acid	Merck	Cat# 402915
Acetonitrile Optima LC/MS grade	Thermo Fisher	Cat# 10489553
Water Optima LC/MS grade	Thermo Fisher	Cat# 10505904
Formic acid	Thermo Fisher	Cat# 10723857
Hexadecyltrimethylammonium bromide (CTAB)	Thermo Fisher	Cat# 10596814
Phenol – chloroform – isoamyl alcohol mixture	Sigma-Aldrich	Cat# 77617
Isopropanol	Fisher Scientific	Cat# 10628143
Sodium acetate (NaOAc)	Sigma-Aldrich	Cat# 32319
Calcium Chloride	Fisher Scientific	Cat# 10171800
PEG4000	Sigma-Aldrich	Cat# 81240
Magnesium sulfate	Fisher Scientific	Cat# 10697412
Sodium phosphate dibasic heptahydrate	Sigma-Aldrich	Cat# S9390
Glucanex	Sigma-Aldrich	Cat# L1412
Hygromycin B	Roche	Cat# 10843555001
Glufosinate ammonium (Basta)	Sigma-Aldrich	Cat# 45520
X-α-gal	Takara	Cat# 630463
Aureobasidin A	Takara	Cat# 630499
DL-Dithiothreitol (DTT)	Sigma-Aldrich	Cat# D9163
EDTA	Sigma-Aldrich	Cat# 60-00-4
Phosphatase inhibitor tablets PhosphoSTOP™	Roche	Cat# 4906845001
Quick Start™ Bradford 1x Dye Reagent	BioRad	Cat# 5000205
4x Laemmli sample buffer	BioRad	Cat# 1610747
Bovine Serum Albumin (BSA)	Sigma-Aldrich	Cat# A9647

(Continued on next page)

Continued

REAGENT or RESOURCE	SOURCE	IDENTIFIER
Tween20	Sigma-Aldrich	Cat# P2287
cOmplete™ EDTA-free protease inhibitor cocktail	Roche	Cat# 11873580001
GFP-Trap® agarose beads	ChromoTek	Cat# gta
ATP	Sigma-Aldrich	Cat# A7699
SuperSignal™ West Femto Maximum Sensitivity Substrate	Thermo Scientific	Cat# 34096

Critical commercial assays

C18 SepPak columns	Waters	Cat# WAT020805
C18 microspin columns	The Neast Group	Cat# 74-4601
Mobicol columns	2B Scientific	Cat# M1002
Filter (small) 10 um pore size	2B Scientific	Cat# M2110
In-Fusion HD Cloning Kit	Takara	Cat# 639650
GoScript™ Reverse Transcription System	Promega	Cat# A5000
Qubit BR assay	Thermo Fisher	Cat# Q32850
Frozen-EZ Yeast Transformation II™	Zymo Research	Cat# T2001
Trans-Blot Turbo RTA Mini 0.2 μm PVDF transfer kit	BioRad	Cat# 1704272
RNeasy Plant Mini Kit	QIAGEN	Cat# 74904
Pierce™ ECL Western Blotting Substrate	Thermo Scientific	Cat# 32106

Deposited data

Appressorium phosphoproteomics DDA data	This paper	Pride: PXD044830
Appressorium phosphoproteomics PRM data	This paper	Panorama: PXD044865

Experimental models: Organisms/strains

<i>Magnaporthe oryzae</i> Guy11	Leung et al. ⁶⁶	N/A
$\Delta pmk1$	Xu and Hamer ⁵	N/A
$\Delta pmk1$:Pmk1-GFP	Sakulkoo et al. ⁶	N/A
Guy11:ToxA:GFP	Ryder et al. ³	N/A
$pmk1^{AS}$	Sakulkoo et al. ⁶	N/A
Guy11: Vts1-GFP	This paper	N/A
$\Delta vts1$:Vts1	This paper	N/A
$\Delta vts1$:Vts1 ^{A175}	This paper	N/A
$\Delta vts1$:Vts1 ^{D175}	This paper	N/A
$\Delta vts1$:Vts1 ^{A420}	This paper	N/A
$\Delta vts1$:Vts1 ^{D420}	This paper	N/A
<i>Oryza sativa</i> cultivar CO-39	Talbot et al. ⁶⁷	N/A

Oligonucleotides

Primers are listed in Table S1	This paper	N/A
------------------------------------------------	------------	-----

Recombinant DNA

pScBAR-Vts1-GFP	This paper	N/A
pScBAR-Vts1 ^{A175}	This paper	N/A
pScBAR-Vts1 ^{D175}	This paper	N/A
pScBAR-Vts1 ^{A420}	This paper	N/A
pScBAR-Vts1 ^{D420}	This paper	N/A
MEK2 ^{DD}	Menke et al. ⁷¹	N/A
MPK6	Menke et al. ⁷¹	N/A
pOPINJ-Pmk1	This paper	N/A
pOPINF-Vts1	This paper	N/A
pGADT7-Pmk1	Óses-Ruiz et al. ⁷	N/A
pGBKT7-Mst12	Óses-Ruiz et al. ⁷	N/A
pGBKT7-14-3-4	This paper	N/A

(Continued on next page)

Continued

REAGENT or RESOURCE	SOURCE	IDENTIFIER
pGBKT7-MGG_00345	This paper	N/A
pGBKT7-MGG_00454	This paper	N/A
pGBKT7-MGG_00800	This paper	N/A
pGBKT7-MGG_00803	This paper	N/A
pGBKT7-MGG_01279	This paper	N/A
pGBKT7-MGG_01311	This paper	N/A
pGBKT7-MGG_01376	This paper	N/A
pGBKT7-MGG_01836	This paper	N/A
pGBKT7-MGG_03139	This paper	N/A
pGBKT7-MGG_03196	This paper	N/A
pGBKT7-MGG_03218	This paper	N/A
pGBKT7-MGG_03558	This paper	N/A
pGBKT7-MGG_04708	This paper	N/A
pGBKT7-MGG_04790	This paper	N/A
pGBKT7-MGG_05199	This paper	N/A
pGBKT7-MGG_05220	This paper	N/A
pGBKT7-MGG_06258	This paper	N/A
pGBKT7-MGG_06334	This paper	N/A
pGBKT7-MGG_06393	This paper	N/A
pGBKT7-MGG_06403	This paper	N/A
pGBKT7-MGG_06726	This paper	N/A
pGBKT7-MGG_07667	This paper	N/A
pGBKT7-MGG_07714	This paper	N/A
pGBKT7-MGG_08061	This paper	N/A
pGBKT7-MGG_08097	This paper	N/A
pGBKT7-MGG_09293	This paper	N/A
pGBKT7-MGG_09554	This paper	N/A
pGBKT7-MGG_09697	This paper	N/A
pGBKT7-MGG_09898	This paper	N/A
pGBKT7-MGG_10538	This paper	N/A
pGBKT7-MGG_12865	This paper	N/A
pGBKT7-MGG_14847	This paper	N/A

Software and algorithms

tidyverse	Wickham et al. ⁸¹	https://www.tidyverse.org/
ImageJ	NIH	https://imagej.net/
BioRender	Biorender	https://biorender.com/
GraphPad Prism 8	GraphPad	https://imagej.nih.gov/ij/
MSConvert package	Matrix Science	https://proteowizard.sourceforge.io/
Mascot server v.2.4.1	Matrix Science	https://www.matrixscience.com/search_form_select.html
Scaffold v.5	Proteome Software	https://www.proteomesoftware.com/products/scaffold-5
Proteome Discoverer 2.5	Thermo Fisher Scientific	Cat# OPTON-31014

RESOURCE AVAILABILITY

Lead contact

Frank L.H. Menke (frank.menke@tsl.ac.uk) is the lead contact for MS-related data, proteomics resources, biological materials, and fungal strains.

Materials availability

Plasmids and *M. oryzae* strains generated in this study will be made available upon request from the [lead contact](#).

Data and code availability

- The DDA proteomics data have been deposited to the ProteomeXchange Consortium via the PRIDE⁶⁴ partner repository with the dataset identifier Pride: PXD044830 and targeted proteomic data via Panorama⁶⁵ with dataset identifier Panorama: PXD044865.
- Original source code for the data analysis in this paper can be found at https://github.com/TeamMacLean/NCM_NT_1705_22022023_PHOS_SITE_CONS
- Any additional information required to reanalyze the data reported in this paper is available from the [lead contact](#) upon request.

EXPERIMENTAL MODEL AND STUDY PARTICIPANT DETAILS

Magnaporthe oryzae and growth conditions

Magnaporthe oryzae strains (isolate Guy11⁶⁶) used in this study were routinely grown on agar plates with solid complete medium. Fungal strains were incubated at 26°C with a 12 h light and dark cycle.⁶⁷ For long-term storage, *M. oryzae* strains were grown over sterile filter paper discs (Whatman International) placed on complete medium agar plates. The paper discs were then dehydrated and stored at -20°C.

Oryza sativa and growth conditions

Blast susceptible rice (*Oryza sativa*) cultivar CO-39 plants were used in this study. Plants were grown in controlled environment rooms at 26°C day temperature and 24 °C night temperature, 16-hour light period, and 85% humidity.^{67,68}

METHOD DETAILS

In vitro appressorium assay

Conidia were harvested from a Petri dish culture using a sterile disposable plastic spreader in 3 mL sterile distilled water from 8–12 days old cultures grown on CM agar. The conidial suspension was filtered through sterile Miracloth (Calbiochem) and fractionated by centrifugation at 5000 x g (Beckman, JA-17) for 15 min at room temperature. The pellet of conidia was re-suspended in 0.2 % (w/v) gelatin (BDH) and the spore concentration determined using a haemocytometer (Improved Neubauer). Spores were diluted to a final concentration of 5 x 10⁴ conidia mL⁻¹. Conidia were quantified and then diluted in sterile water to 7.5 x 10⁵ conidia/mL in the presence of 50 ng/μL 1,16-Hexadecanediol (Sigma). For microscopic observations, a 50 μL aliquot of conidial suspension was inoculated onto a borosilicate glass coverslip (Menzel-Gläser, Fisher Scientific UK Ltd.) and placed on a moist paper towel. Conidia were incubated at 24 °C and observed as indicated. For large-scale conidial germination assays, conidial suspensions were poured into square petri plates (12 cm X 12 cm X 1.7 cm) (Greiner Bio One) to which 10 glass cover slips (Menzel-Gläser, Fisher Scientific UK Ltd.) were attached by adhesive. Appressorium formation was monitored under a Will-Wetzlar light inverted microscope (Wilovert®, Hund Wetzlar, Germany) for ensuring homogeneous and synchronized infection structure formation. Samples were collected as indicated by scraping the surface of the coverslips with a sterile razor blade (Fisher Scientific, UK). Harvested samples were immediately frozen in liquid nitrogen and stored at -80 °C for subsequent protein extraction.

Protein extraction and phosphopeptide enrichment

Spores and appressoria samples were lyophilized and resuspended in extraction buffer (Urea 8M, NaCl 150 mM, Tris pH 8 100 mM, EDTA 5 mM, 1x protease inhibitor cocktail (Sigma)) for mechanical disruption using GenoGrinder 2010 (Thermo Scientific) in cold conditions (1 min at 1200 rpm). The homogenate was centrifuged for 10 min at 16,000 x g (Eppendorf 5415D microcentrifuge). The supernatant was used for phosphopeptide enrichment. Sample preparation started from 1.5 mg of protein extract (determined using the Bradford assay) dissolved in ammonium bicarbonate buffer containing 8 M urea. First, the protein extracts were reduced with 5 mM Tris (2-carboxyethyl) phosphine (TCEP) for 30 min at 30°C with gentle shaking, followed by alkylation of cysteine residues with 40mM iodoacetamide at room temperature for 1 hour. Subsequently, the samples were diluted to a final concentration of 1.6 M urea with 50mM ammonium bicarbonate and digested overnight with trypsin (Promega; 1:100 enzyme to substrate ratio). Peptide digests were purified using C18 SepPak columns as described before.⁵¹ Phosphopeptides were enriched using titanium dioxide (TiO₂, GL Science) with phthalic acid as a modifier as described previously.⁶⁹ Phosphopeptides were eluted by a pH-shift to pH 10.5 and immediately purified using C18 microspin columns (The Nest Group Inc., 5 – 60 μg loading capacity). After purification, all samples were dried in a Speedvac, stored at -80°C and re-suspended in 2% Acetonitrile (AcN) with 0.1% trifluoroacetic acid (TFA) just before the mass spectrometric measurement.

Mass-Spectrometry analysis

LC-MS/MS analysis was performed using an Orbitrap Fusion trihybrid mass spectrometer (Thermo Scientific) and a nanoflow-UHPLC system (Dionex Ultimate3000, Thermo Scientific). Peptides were trapped to a reverse phase column (Acclaim PepMap, C18 5 μm , 100 μm x 2 cm, Thermo Scientific) connected to an analytical column (Acclaim PepMap 100, C18 3 μm , 75 μm x 50 cm, Thermo Scientific). Peptides were eluted in a gradient of 3–40 % acetonitrile in 0.1 % formic (solvent B) acid over 120 min followed by gradient of 40–80 % B over 6 min at a flow rate of 200 nL/min at 40°C. The mass spectrometer was operated in positive ion mode with nano-electrospray ion source with ID 0.02mm fused silica emitter (New Objective). Voltage +2200 V was applied via platinum wire held in PEEK T-shaped coupling union with transfer capillary temperature set to 275 °C. The Orbitrap, MS scan resolution of 120,000 at 400 m/z, range 300 to 1800 m/z was used, and automatic gain control (AGC) was set at $2e^5$ and maximum inject time to 50 ms. In the linear ion trap, MS/MS spectra were triggered with data dependent acquisition method using ‘top speed’ and ‘most intense ion’ settings. The selected precursor ions were fragmented using Higher-energy collisional dissociation (HCD) with collision energy set at 30%. Dynamic exclusion was set to 15 seconds after 2 round of fragmentation per precursor. Charge state allowed between 2+ and 7+ charge states to be selected for MS/MS fragmentation.

Plasmid construction

Polymerase chain reaction (PCR) products were amplified from *M. oryzae* DNA, cDNA or plasmid templates using primers listed in Table S1. Point mutations were generated using site-directed mutagenesis primers listed in Table S1. Genes of interest were cloned into pScBar-GFP for protein pulldowns, into pGBKT7 for Y2H assays, and pOPIN vectors (Berrow et al., 2007) for protein production in *E. coli* by the In-Fusion™ cloning system (Takara Bio, USA). Sequences were amplified with primers containing homologous overhang sequences matching the cloning plasmid (Table S1). Cloning reactions were performed using 1 μL 5x In-Fusion® HD enzyme premix combined with 100 ng of linearized vector and 50–100 ng of purified PCR fragment in a total reaction volume of 5 μL . After incubation at 42 °C for 30 min, the reaction was transformed into *E. coli* Stellar™ (Takara Bio) competent cells. The sequences of all genes were verified by Sanger sequencing.

DNA purification

For large-scale DNA extraction, fungal mycelium was generated by growing fungal culture on either cellophane discs or liquid as previously described.⁶⁸ Using a mortar and pestle, 7–12 days old mycelium was ground into powder. Mycelial powder was decanted to a 1.5 mL microcentrifuge tube and mixed with 500 μL of pre-warmed CTAB (2% (w/v) Hexadecyltrimethylammonium Bromide (CTAB), 100 mM Tris base, 10 mM EDTA and 0.7 M NaCl) and incubated at 65°C with gentle mixing every 10 min. An equal volume of chloroform isoamyl alcohol (CIA) was added, mixed thoroughly, and incubated with shaking for 30 min at room temperature. This was followed by centrifugation at 17000 x g for 10 min. This step was repeated twice by adding equal volumes of CIA and mixing vigorously on a shaker before centrifugation. The final supernatant was transferred into a clean sterile microcentrifuge tube and of isopropanol (2 x vol) added before incubating at -20°C overnight. The samples were centrifuged at 17000 x g for 10 min and the supernatant (isopropanol) was gently removed and the resulting pellet re-suspended in 500 μL sterile distilled water (SDW) and left to dissolve at room temperature with gentle tapping to mix. Sodium acetate (NaOAc) (0.1 vol) and 100% ethanol (2 vol) were added to re-precipitate nucleic acids. The mixture was incubated at -20°C for 2 h and pelleted by centrifugation at maximum speed, before washing with 400 μL of 70% (v/v) ethanol. The DNA was re-suspended in nuclease-free water. RNase (2 μL) was added and incubated at 37°C for 1 h to digest contaminating RNA.

Southern blotting

Southern blot analysis was used to determine positive *M. oryzae* null mutants for the *VTS1* gene. DNA digestion of *M. oryzae* transformants was performed overnight using *Hind*III endonuclease and subsequently fractionated by electrophoresis in an agarose gel at 100V. Fragments of genomic DNA were separated in agarose gels were transferred to Hybond-NX (Amersham Biosciences). Prior to blotting, partial depurination of DNA molecules was performed to enhance DNA transfer by submerging the agarose gel in 0.25 M with gentle rocking. Gels were then neutralized by replacing HCl with 0.4 M NaOH. For transfer of DNA from the agarose gel to the positively charged membrane, blots were carried out using a 0.4M NaOH transfer buffer that was drawn through a wet paper wick (Whatman/international) supported by a Perspex panel onto which the agarose gel was placed. A sheet of Hybond-NX membrane was then laid on the gel and positions of the wells were pencil marked. Three layers of Whatman 3MM paper and a stack of paper towels (Kimberley Clark Corporation) were laid over the membrane followed by a glass plate and a 500 g weight were placed on the stack as a weight. The transfer was left at room temperature overnight. Then, the nucleic acid was fixed to the membrane by UV crosslinking to the membrane with 120 millijoules.cm⁻² using a BLX crosslinker (Bio-Link).

Whole genome sequencing

Purified DNA was obtained using the CTAB procedure, as previously described.⁶⁸ A NanoDrop spectrophotometer (Thermo Scientific) and a Qubit BR assay (Thermo Fischer) were used to analyze template quality and determine the concentration of double-stranded DNA. Sequencing was carried out using Novogene Sequencing services (Cambridge, UK). Whole

genome sequencing was performed on NovaSeq 6000 system (Illumina), with two lanes per sample. BAM files were created by using bowtie2 for aligning raw reads to the *M. oryzae* reference genome 70-15. Finally, the IGV viewer was used for the visualization of the generated BAM files.

Protoplast-mediated transformation of *M. oryzae*

A section of 2.5 cm² mycelium from a *M. oryzae* plate culture (8–10 days-old) was blended in 150 mL CM liquid and incubated at 25°C, shaking (125 rpm) in an orbital incubator for 48h. Fresh ST (sucrose, 0.6M, Tris-HCl 0.1 M (pH 7), STC (sucrose, 1.2 M, Tris-HCl, 10 mM (pH 7.5)) and PTC (PEG4000, 60%, Tris-HCl, 10 mM (pH 7.5), calcium chloride) buffers were prepared and stored at 4°C. The culture was harvested by filtration through sterile Miracloth and the mycelium washed with sterile deionized water (SDW). The mycelium was transferred to a 50 mL falcon tube with 40 mL OM buffer (1.2 M magnesium sulfate, 10 mM sodium phosphate (pH5.8), Glucanex 5% (Sigma)). Mycelium in the falcon tube with OM buffer was shaken gently to disperse hyphal clumps. Then, it was incubated at 30°C with gentle (75 rpm) shaking, for 3 h. The digested mycelium was transferred to two sterile polycarbonate Oakridge tubes (Nalgene) and overlaid with an equal volume of cold ST buffer. Resulting protoplasts were recovered at the OM/ST interface by centrifugation at 5000 x g, for 15 min at 4°C in a swinging bucket rotor (Beckman JS-13.1) in a Beckman J2.MC centrifuge. Protoplasts were recovered and transferred to a sterile Oakridge tube, which was then filled with cold STC buffer. The protoplasts were pelleted at 3,000 x g for 10 min (Beckman JS-13.1 rotor). This wash was carried out twice more with STC, with complete re-suspension of the pellet. After the last wash, protoplasts were resuspended in 1 mL of STC and checked by microscopy. In an Eppendorf tube, an aliquot of protoplasts was combined with 6 µg DNA. The mixture was incubated at room temperature for 30 min. After incubation, 1 mL of PTC was added in 2 aliquots, mixed gently by inversion, and incubated at room temperature for 20 min. The transformation mixture was added to 150 mL of molten agar medium and poured into 5 sterile Petri dishes. For selection of transformants on hygromycin B (Roche), plate cultures were incubated in the dark for at least 16 h at 24°C and then overlaid with approximately 15 mL of OCM/1% agar (CM osmotically stabilized with sucrose, 0.8M) containing 600 µg mL⁻¹ hygromycin B. For selection of glufosinate ammonium (30 µg mL⁻¹) (Basta) resistant transformants, OCM was replaced with BDCM (yeast nitrogen base without amino acids and ammonium sulfate, 1.7 g L⁻¹ (Difco), ammonium nitrate, 2 g L⁻¹ asparagine, 1 g L⁻¹ glucose, 10 g L⁻¹ sucrose, 0.8 (pH 6)).

RNA extraction and cDNA synthesis

Total RNA was isolated from mycelia tissue after 48 h growth on CM liquid culture using RNeasy Plant Mini Kit (QIAGEN) following the manufacturer's instructions. RNA was reversed transcribed to synthesize first-strand cDNA with GoScript™ Reverse Transcription System (Promega) according to the manufacturer's protocol.

Virulence analysis

Conidia were harvested from a Petri dish culture using a sterile disposable plastic spreader in 3 mL sterile distilled water from 8–12 days old cultures grown on CM agar. The conidial suspension was filtered through sterile Miracloth (Calbiochem) and fractionated by centrifugation at 5000 x g (Beckman, JA-17) for 15 min at room temperature. The pellet of conidia was re-suspended in 0.2 % (w/v) gelatin (BDH) and the spore concentration determined using a hemocytometer (Improved Neubauer). Spores were diluted to a final concentration of 5 x 10⁴ conidia mL⁻¹. For spray infection assays, the spore suspension was used to infect rice using an airbrush (Badger). After spray inoculation, the plants were covered in polythene bags and incubated in a controlled plant growth chamber (Conviron) at 24°C for 48 h with a 12 h light and dark cycle, and 85% relative humidity. The inoculated plants were incubated for 5–6 days before scoring the lesions.⁷⁰ For leaf drop assays, the spore suspension was drop-inoculated on detached rice leaves using a micropipette. Rice CO-39 plants were grown for 3 weeks in 9 cm diameter plastic plant pots.

Light microscopy

Differential interference contrast (DIC) microscopy was performed on an IX81 motorized inverted microscope (Olympus) with X100/1.4 or X60/1.35 oil objectives. Images from the microscope were captured using a Photometrics CoolSNAP HQ2 camera system (Roper Scientific) under the control of MetaMorph software package (MDS Analytical Technologies).

Cryo-scanning electron microscopy

The infected rice leaf samples were mounted on an aluminium stub using Tissue Tek^R (BDH Laboratory Supplies, Poole, England). The stub was then immediately plunged into liquid nitrogen slush at approximately -210°C to cryo-preserve the material. The sample was transferred onto the cryo-stage of an ALTO 2500 cryo-transfer system (Gatan, Oxford, England) attached to an FEI Nova NanoSEM 450 (FEI, Eindhoven, The Netherlands). Sublimation of surface frost was performed at -95°C for three minutes before sputter coating the sample with platinum for 3 mins at 10mA, at colder than -110°C. After sputter-coating, the sample was moved onto the cryo-stage in the main chamber of the microscope, held at approximately -125°C. The sample was imaged at 3kV and digital TIFF files were stored.

Yeast-two-hybrid (Y2H) analysis

Desired constructs in pGBKT7 and pGADT7 were co-transformed into chemically competent *Saccharomyces cerevisiae* Y2HGold cells (Takara Bio, USA) using the commercial kit Frozen-EZ Yeast Transformation II™ (Zymo Research, UK) as detailed in the user manual. The Matchmaker® Gold Yeast Two-Hybrid System (Takara Bio USA) was used to detect protein–protein interactions between Pmk1 and its putative targets. Single co-transformed colonies grown on selection plates were inoculated in 5 mL of SD^{-Leu-Trp} and grown overnight at 30 °C. Saturated culture was then used to make serial dilutions of OD₆₀₀ 1, 1⁻¹, 1⁻², 1⁻³, respectively. An aliquot of 5 μL of each dilution was then spotted on a SD^{-Leu-Trp} plate as a growth control, SD^{-Leu-Trp-His} (low stringency media) and SD^{-Leu-Trp-Ade-His} (high stringency media) plate containing X-α-gal (Takara) and aureobasidin A (Takara). Plates were imaged after incubation for 60 – 72 hr at 30 °C.

Recombinant proteins production and purification

Recombinant pOPIN plasmids encoding 6xHisGST-Pmk1 and 6xHis-Vts1, as well as pET-28a vectors encoding 6xHis-MPK6 and 6xHis-MEK2^{DD}⁷¹ were transformed into *E. coli* Rosetta™ (DE3) cells. The bacteria were pre-inoculated in 100 mL of LB medium with carbenicillin and chloramphenicol overnight. An amount of 25 mL culture was then diluted into 1 L of autoinduction media (AIM) (10 g/L tryptone, 5 g/L yeast extract, 3.3 g/L (NH₄)₂SO₄, 6.8 g/L KH₂PO₄, 7.1 g/L Na₂HPO₄, 0.5 g/L glucose, 2 g/L α-lactose, 0.15 g/L MgSO₄ magnesium sulphate and 0.03 g/L trace elements)⁷² with appropriate antibiotics and grown in at 37 °C for 6 h and then 16 °C overnight. Cells were harvested and resuspended in ice-cold lysis buffer (50 mM Tris-HCl pH 8.0, 50 mM glycine, 5% glycerol, 500 mM NaCl and 20 mM imidazole, supplemented with cOmplete™ EDTA-free Protease Inhibitor Cocktail). The cells were then disrupted by sonication using a Vibra-Cell™ sonicator (SONICS) with a single 13 mm probe, with the cells chilled on ice. The sonicator was set at 40 % amplitude, with a 1 s pulse followed by a 3 s pause, for 16 min. After the first sonication cell lysate was stirred and followed by another sonication of 8 min. The soluble fraction of the cell lysate was obtained by centrifuging for 30 min at 36,250 g at 4 °C. The supernatant was transferred to an ÄKTAexpress to carry out immobilized metal affinity chromatography (IMAC) in tandem with gel filtration. IMAC was carried out using 5 mL HisTrap™ HP NTA columns (GE Healthcare). After washing with 100 mL of washing buffer (50 mM Tris-HCl pH 8.0, 50 mM glycine, 5% glycerol, 500 mM NaCl and 20 mM imidazole), proteins were then eluted with 25 mL of elution buffer (50 mM Tris-HCl pH 8.0, 50 mM glycine, 500 mM NaCl, 500 mM imidazole, 5% (v/v) glycerol). This elution was then loaded onto a gel filtration Superdex™ 200 HiLoad™ 26/600 column (GE Healthcare) equilibrated with gel filtration buffer (20 mM HEPES pH 7.5 and 150 mM NaCl). The gel filtration buffer for 6xHisGST-Pmk1 proteins was supplemented with 1 mM TCEP. Protein samples were separated by size and fractionated in 2 mL fractions that were analyzed by SDS-PAGE to assess the presence of proteins. Fractions containing the proteins of interest were pooled and concentrated to 1 mL using VivaSpin® concentrators (Sartorius) with an appropriate molecular weight cut-off. Recombinant proteins were aliquoted and frozen in liquid nitrogen for storage at -80 °C.

Protein extraction and Co-immunoprecipitation (Co-IP) assay

Co-IP experiments were performed to validate Pmk1 - Vts1 interactions during appressorium development. *M. oryzae* appressorium samples of 4 h development transformed were generated for *ToxA*:GFP and *VTS1*-GFP. Total protein was extracted from each frozen sample using mortar and pestle to ground into fine powder. Appressorium powder was mixed with 2x w/v ice-cold extraction buffer (10% glycerol, 25 mM Tris pH 7.5, 1 mM EDTA, 150 mM NaCl, 2% w/v PVPP, 10 mM DTT, 1x protease inhibitor cocktail (Sigma), 0.1% Tween 20 (Sigma)) and vortexed vigorously. After centrifugation at 4,200 x g/4 °C for 20-30 min, the supernatant was used to determine the protein concentration by the Bradford assay. The presence of each protein in the input was determined by SDS-PAGE/Western blot. *ToxA*:GFP and *Vts1*-GFP proteins were detected by probing the membrane with anti-GFP horseradish peroxidase (HRP)-conjugated antibody (Santa Cruz Biotechnology), Pmk1 with a Phospho-p44/42 MAPK (Erk1/2) (Thr202/Tyr204) (D13.14.4E) antibody (Santa Cruz Biotechnology) and a HRP-conjugated anti-rabbit antibody (Abcam). *M. oryzae* actin protein was used as loading control and detected with an anti-actin primary antibody (Agrisera com) and the anti-rabbit HRP conjugated antibody.

For immunoprecipitation, 1 μg of total protein was incubated with 30 μL of GFP beads (ChromoTek) in a rotatory mixer at 4 °C. After 3 h, the beads were pelleted (800 x g, 1 min) and the supernatant removed. The pellet was washed and resuspended in 1 mL of IP buffer (10% glycerol, 25 mM Tris pH 7.5, 1 mM EDTA, 150 mM NaCl, 0.1% Tween 20 (Sigma)) and pelleted again by centrifugation as before. Washing steps were repeated five times. Finally, 30 μL of 1:1 dilution of SDS buffer and water supplemented with 100 mM DTT was added to the beads and incubated for 10 min at 70 °C. The beads were pelleted again, and the supernatant loaded onto SDS-PAGE gels prior to Western blotting. Membranes were probed with anti-GFP and a Phospho-p44/42 MAPK (Erk1/2) (Thr202/Tyr204) (D13.14.4E) antibody as described before. Blots membrane imaging was carried out with an ImageQuant LAS 4000 luminescent imager (GE Healthcare Life Sciences).

To confirm Vts1-GFP bait protein, LC-MS/MS analysis was performed Vts1-GFP pulled down and excised from a SDS-PAGE gel. Briefly, gel pieces were excised into 2x2mm and washed three times with acetonitrile, 50 mM ammonium bicarbonate, pH 8.0 (v/v), followed by shrinking with acetonitrile. Gel pieces were reduced with freshly made 10 mM DTT for 30 min at 37 °C followed by alkylation with 55 mM chloroacetamide for 20 min at room temperature. Gel pieces were subjected to three more washes with acetonitrile, 50 mM ammonium bicarbonate, pH 8.0 (v/v), followed by shrinking with acetonitrile. The last step included Trypsin Gold (Promega) at a concentration of 10 ng/μL. In-gel trypsin digestions were carried out at 37 °C overnight.

In vitro phosphorylation assay

For *in vitro* phosphorylation assays, 6xHis-GST tagged Pmk1 (250ng) was activated by incubation with recombinant MEK2^{DD} (250ng). Recombinant 6xHis tagged Vts1 (500ng) was incubated with active Pmk1 in kinase buffer (25mM Tris pH 7.5, 10mM MnCl₂, 1mM EGTA and 1mM DTT) in the presence of 1 mM ATP at 30 °C for 30 min. Proteins were separated by SDS-PAGE and transferred to a polyvinylidene difluoride (PVDF) membrane using a Trans-Blot turbo transfer system (Bio-Rad). PVDF membrane was blocked with 2% bovine serum albumin (BSA) in Tris-buffered saline and 1% Tween 20. His tag detection was carried using polyclonal anti-6xHis horseradish peroxidase (HRP)-conjugated antibody (Abcam). Pmk1 activated was detected using Phospho-p44/42 MAPK (Erk1/2) (Thr202/Tyr204) (Santa Cruz Biotechnology) and anti-rabbit HRP-conjugated antibodies. Vts1 phosphorylation was detected using pS/pT - P antibody (Abcam). Pierce™ ECL Western Blotting Substrate (Thermo Fisher Scientific) was used for detection. Membranes were imaged using ImageQuant LAS 4000 luminescent imager (GE Life Sciences). Phosphorylation assays were analyzed by mass spectrometry.

Generation of schematics

The schematics in this paper were created with BioRender.

QUANTIFICATION AND STATISTICAL ANALYSIS

Functional categorization of Pmk1 targets

To further understand the putative direct Pmk1 targets obtained from the MS approach, selected phosphoproteins containing a MAPK phosphorylation motif (Pxx[S/T]P or [S/T]P) were categorized based on functional annotations from Blast2GO⁷³ and Pfam.⁷⁴

Spectral library generation and raw data processing

Peak lists in the format of Mascot generic files (.mgf files) were prepared from raw data using MSConvert package (Matrix Science). Peak lists were searched on Mascot server v.2.4.1 (Matrix Science) against either *Magnaporthe oryzae* (isolate 70-15, version 8) database, an in-house contaminants database. Tryptic peptides with up to 2 possible mis-cleavages and charge states +2, +3, +4, were allowed in the search. The following modifications were included in the search: oxidized methionine, phosphorylation on Serine, Threonine, Tyrosine as variable modification and carbamidomethylated cysteine as static modification. Data were searched with a mono-isotopic precursor and fragment ions mass tolerance 10ppm and 0.6 Da respectively. Mascot results were combined in Scaffold v. 5 (Proteome Software), with the following settings, protein threshold 95%, 1 peptide minimum per protein and 80% peptide threshold, resulting in a Peptide FDR below 0.05. Data were exported to Excel (Microsoft Office) to prepare the precursor lists for PRM.

Label free quantification at MS1 level

Peptide quantification was performed as described recently⁷⁵ with the following modifications. Raw data files were processed using Proteome Discoverer 2.5 (Thermo Fisher Scientific) and searched against an in-house constructs and contaminants database and the *Magnaporthe oryzae* (isolate 70-15 version 8) database. The processing workflow was made up of the Sequest HT search engine, Percolator (for target/decoy selection) and IMP-ptmRS (to calculate modification site probabilities). Tryptic peptides with up to 2 possible mis-cleavage and charge states +2, +3 were allowed in the search and the following modifications were included in the search: carbamidomethylated Cysteine (fixed), oxidized Methionine (variable) and phosphorylated Serine, Threonine and Tyrosine (variable). Maximum number of the same variable modification per peptide was limited to 3 and total number of variable modifications to four per peptide. Data were searched with a mono-isotopic precursor and fragment ion mass tolerance 10 ppm and 0.6 Da respectively. Peptides were quantified using the 'basic modification analysis' consensus workflow provided by Proteome Discoverer 2.5 and expressed as abundance ratios. Peptides in the Peptide groups tab in the results files were filtered for 'phospho' and reliable and detectable 'quan' values. Threshold for differential phosphopeptides was set at minimum 2-fold change in abundance ratio and an adjusted abundance ratio p-value of less than 0.05. For hypothesis testing a background based t-test was selected. Data for Peptide groups were exported to Excel and further processed in R to visualize the data and generate a heatmap shown in Figure 2. The full data analysis in R can be found on Github using the link provided in the section describing differential phosphosite analysis.

Phosphosite conservation analysis

To determine the conservation of phosphosites across species, a list of 41 fungi of various lifestyles was prepared, and the protein sequences for a given assembly downloaded from the sources listed in Table S1. These were then used in Orthofinder version 2.3.7⁷⁶ and Running diamond 2.0.14⁷⁷ to compute orthogroups and species trees. Each *M. oryzae* phos-site was taken in turn and the orthologues of the source protein were compared to it in turn using blastp from BLAST+2.9.0.⁷⁸ If any matches were found according to BLAST defaults, the best HSP (by bitscore) was retained and the HSP in the orthologue was extended to match the full range of the length of the *M. oryzae* phosphopeptide sequence. If the phos-site lies in the range of the HSP, the orthologue was then checked to see whether the corresponding residue in the orthologue has a match to the *M. oryzae* phos-site residue. The complete analysis, scripts, result files and graphics generated in R can be found at https://github.com/TeamMacLean/NCM_NT_1705_22022023_PHOS_SITE_CONS

Clustering of phosphosites by conservation

For each phospho-site and query fungal species, the proportion of *M. oryzae* sites matched was calculated and tabulated for *k*-means clustering. The value of *k* was determined by scanning values of *k* from 2 to 50 and calculating the variance as Within Sum of Squares at each *k*. The variance in clusters stopped decreasing noticeably at about *k* = 9 and that was taken as the value of *k* for final clustering. *K* means clustering was performed using the Factoextra package⁷⁹ *kmeans* function in R⁸⁰ version 4.2.0. Data preparation was performed in R using the Tidyverse packages.⁸¹ Heatmaps were prepared using ComplexHeatmap.⁸² Phylogenetic trees were analyzed in ape,⁸³ dendextend⁸⁴ and rendered in ggtree.⁸⁵

Clustering and GO analysis

M. oryzae Gene Ontology analysis was performed using the version MG8 annotations from ENSEMBL BioMart. Cluster enrichment computations were performed in the R package clusterProfiler 4.6.2⁸⁶ at a *p*-value of ≤ 0.05 with Benjamini-Hochberg corrections for multiple hypothesis tests.

Parallel Reaction Monitoring (PRM)

Peptide quantitation was performed using Parallel Reaction Monitoring (PRM) as described previously.⁸⁷ Briefly, mass to charge ratios (*m/z*) corresponding to selected phospho-peptides were monitored and filtered by the first quadrupole and fragment ions were scanned out in the orbitrap mass analyzer over the duration of the elution profile. The PRM assay also included a selection of in house selected endogenous control peptides (Data S5) having similar relative intensities in each sample and used to measure relative phospho-peptide content. Phosphopeptides with up to three phosphorylated residues were included and total maximum number of variable modifications limited to four. Raw data were peak picked and searched against the data bases on the Mascot server as described above and combined with chromatographic profiles in Skyline⁸⁸ to determine individual peptide intensities. Extracted phospho-peptides intensity were normalized against the summed control peptide intensities to correct for differences in phospho-peptide yield. The assay was performed once for each of three biological replicates and results were subjected to differential phosphosite analysis.

Differential phosphosite analysis

To determine whether phosphosites were differentially abundant between samples for 3 biological replicates we prepared PRM data by replacing missing values with the lowest observed intensity in the data set and then performed a bootstrap *t*-test with 1000 bootstrap resamples with replacement for each phosphosite using the MKInfer package.⁸⁹ We used $p \leq 0.05$ as a threshold for differential abundance. The complete analysis, scripts, result files and graphics generated in R can be found at https://github.com/TeamMacLean/PD_PRO_1499_06122021_PRM2.

Supplemental figures

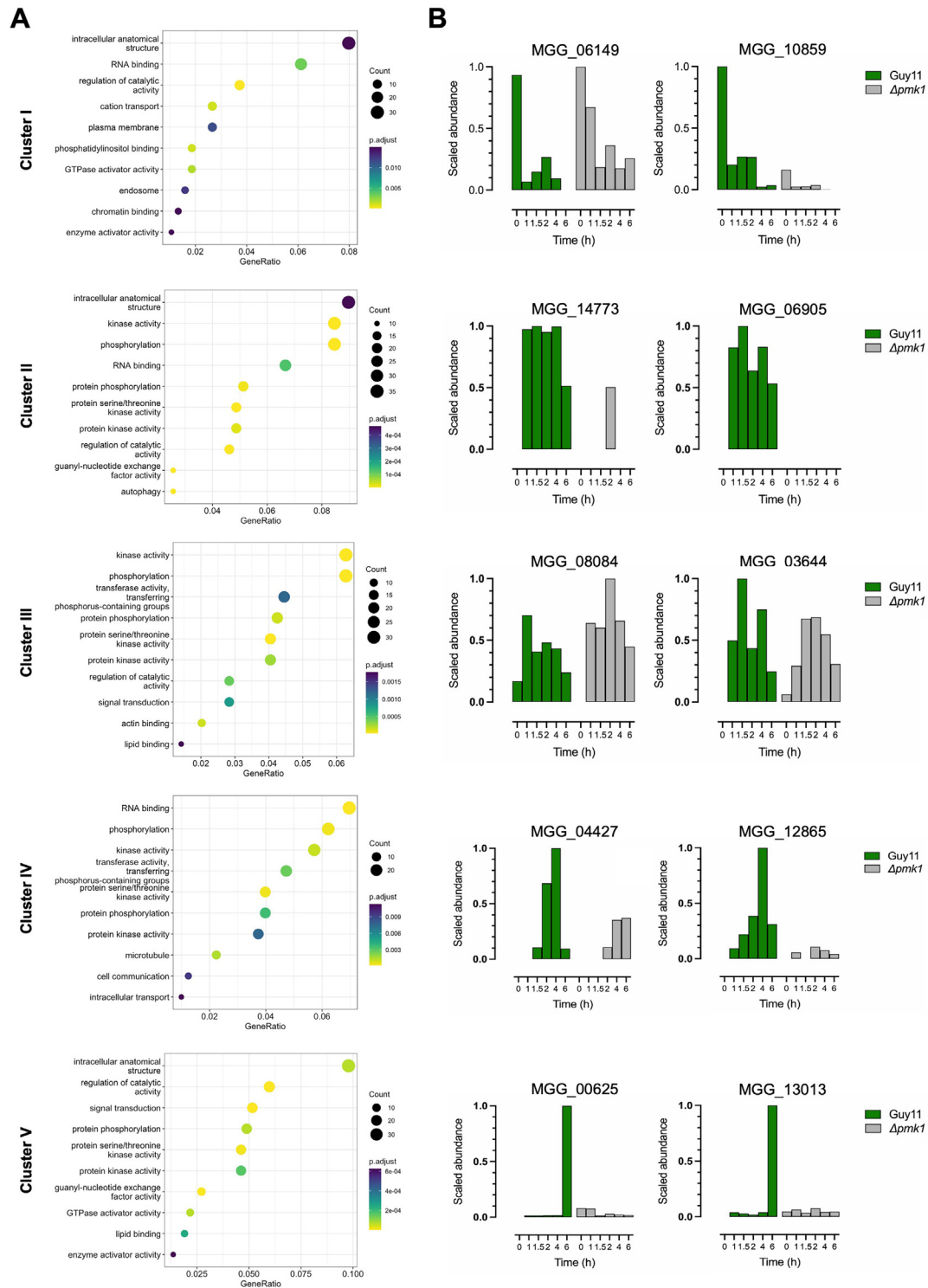


Figure S1. GO-term enrichment for differentially phosphorylated proteins (MS1 analysis), related to Figure 2B

(A) GO term analysis of differentially phosphopeptides analyzed by MS1, categorized according to the time point at which they passed significance threshold. (B) Relative phosphorylation for representative phosphopeptides in each defined cluster. Cluster I, MGG_05433 and MGG_10859; cluster II, MGG_14773 and MGG_06905; cluster III, MGG_08084 and MGG_03644; cluster IV, MGG_04427 and MGG_12865; and cluster V, MGG_00625 and MGG_13013.

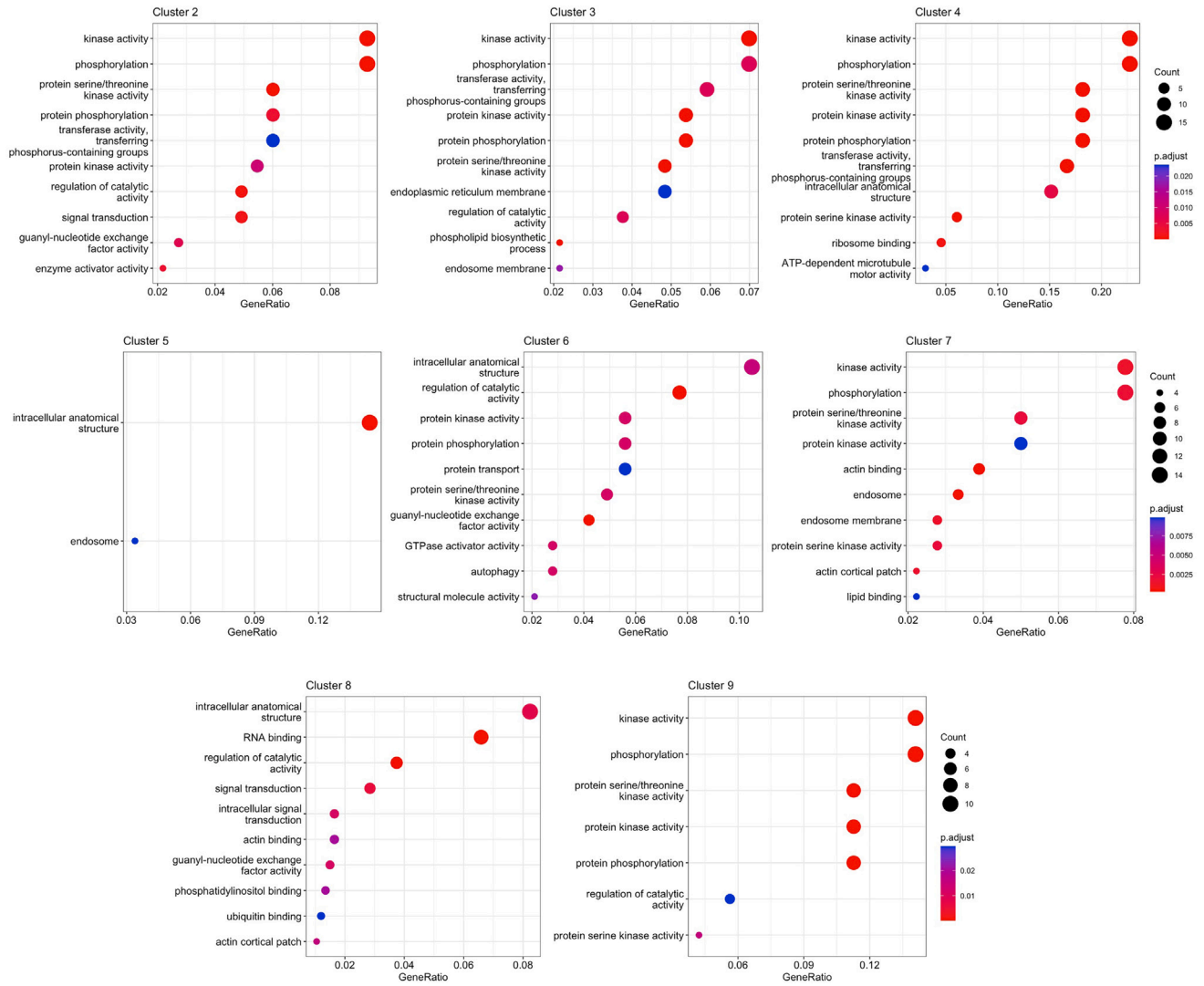


Figure S2. GO-term enrichment for the CPR groups, related to Figure 3B

GO term analysis of evolutionarily conserved phosphopeptides analyzed by MS1, categorized according to the time point at which they passed significance threshold.

Figure S3. Phosphorylation profile of early appressorium development pathways, related to [Figure 4](#)

Heatmap to show relative intensities of differentially phosphorylated peptides in Guy11 and $\Delta pmk1$, clustered by signaling pathway. MGG number, gene name, and phosphosite detected are shown.

Figure S4. Quantitative phosphoproteomics defines putative targets of the Pmk1 MAPK pathway, related to [Figure 5B](#)
Heatmap to show relative intensities of 181 differentially phosphorylated peptides in Guy11 and $\Delta pmk1$. MGG number, gene name, and phosphosite detected are shown.

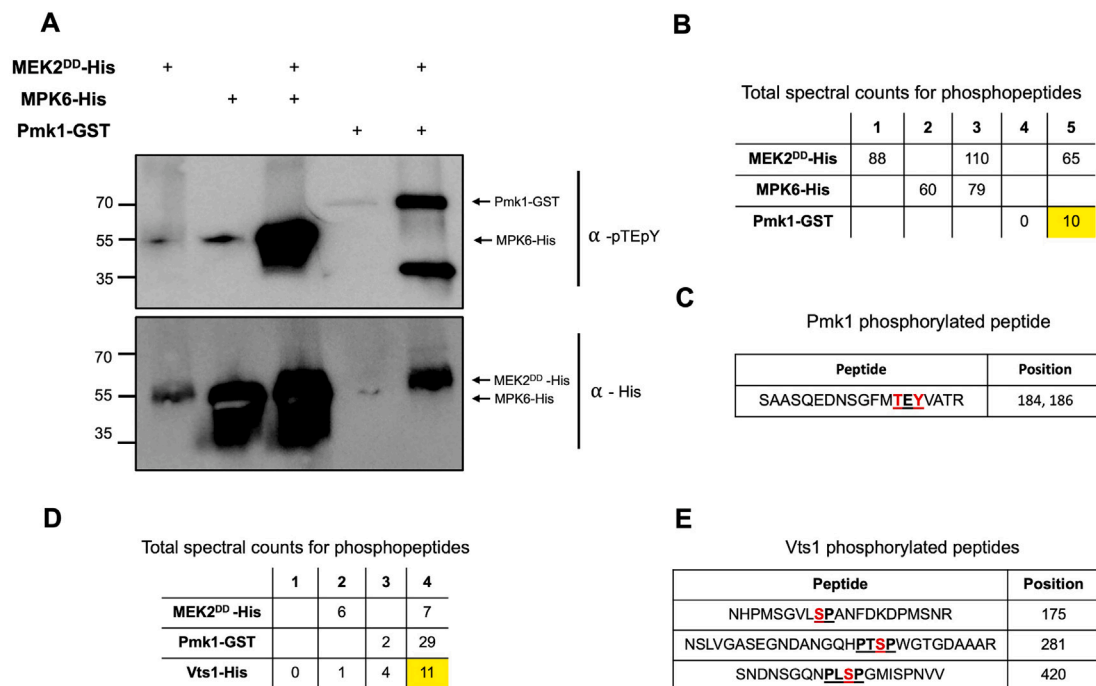


Figure S5. MEK2^{DD} activates *in vitro* Pmk1 on its TEY motif, related to Figure 6B

(A) Western blot analysis of *in vitro* phosphorylation experiment between MEK2^{DD} (N-terminally tagged with 6xHis) and Pmk1 (N-terminally tagged with GST). The previously reported MEK2^{DD} phosphorylation of MPK6 (N-terminally tagged with 6xHis) was used as a positive control. Proteins were immunoblotted with appropriate antisera (listed on the right). Arrows indicate expected band sizes.

(B) Phosphopeptides identified by LC-MS for the *in vitro* kinase assay.

(C) Phosphorylation sites (in red) identified by LC-MS on the Pmk1 MAPK.

(D) Phosphopeptides identified by LC-MS for the *in vitro* kinase assay.

(E) Phosphorylation sites (in red) identified by LC-MS on Vts1.

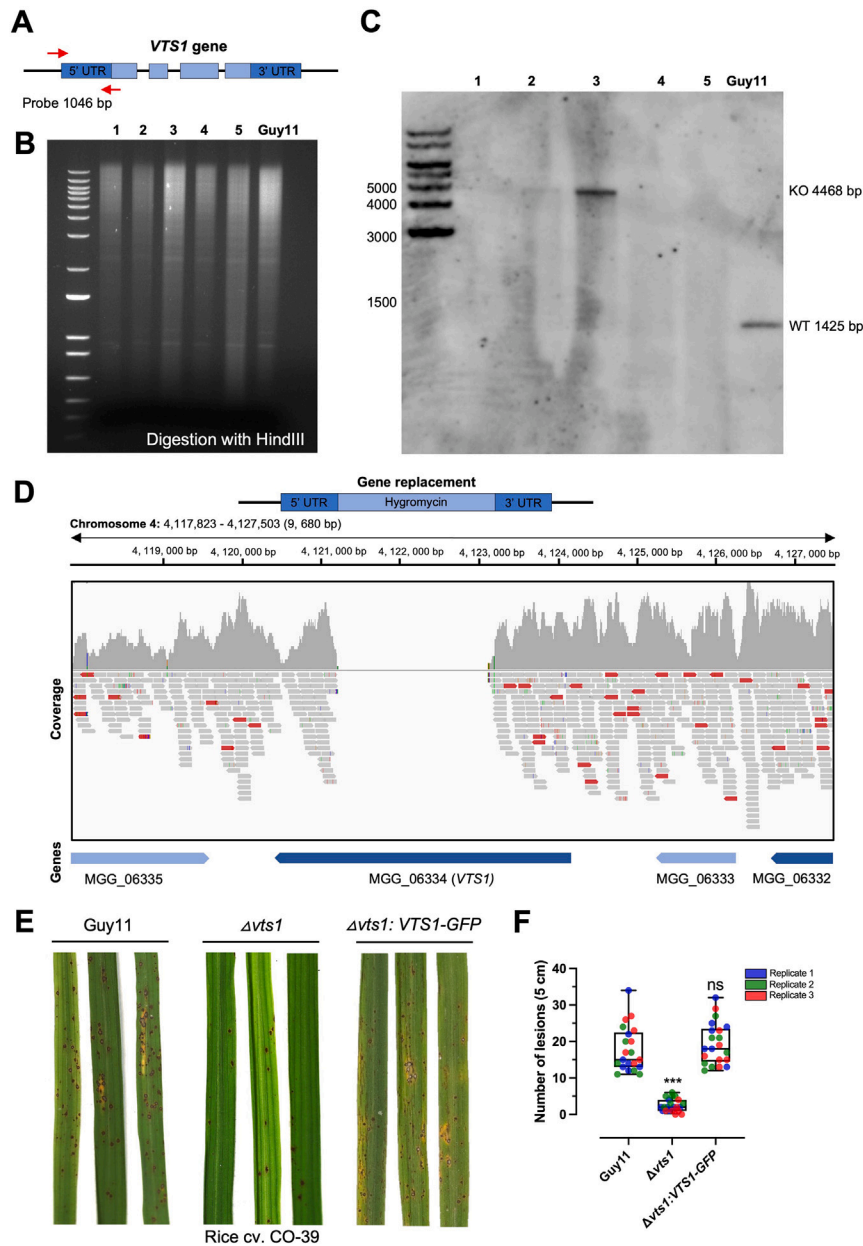


Figure S6. *Vts1* null mutant is necessary for rice blast disease, related to Figures 6F–6I

(A) A probe of 1,046 bp was generated to hybridize to the *VTS1* gene in its 5' UTR region.

(B) Genomic DNA of the putative transformants was digested with *Hind*III, gel fractionated, and transferred to Hybond-NX.

(C) Southern blot analysis showing a single band of 4,468 bp for positive null mutants (KO) and 1,425 bp for wild-type (WT) strains. The blot was probed with 1,046 bp DNA fragment specific to *VTS1*.

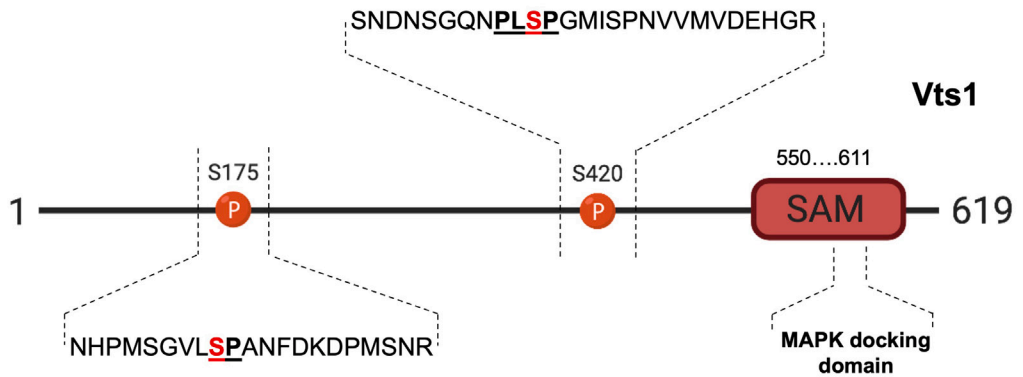
(D) Bioinformatic analysis of one positive $\Delta vts1$ null mutant showing the absence of coverage (reads) for the *VTS1* gene due to the presence of the *HPH* cassette inserted by the split marker strategy.

(E) 2-week-old seedlings of rice cultivar CO-39 were spray inoculated with equal amounts of conidial suspensions of Guy11 and $\Delta vts1$ containing 10^5 conidia mL^{-1} in 0.2% gelatin. Seedlings were incubated for 6 days to develop blast disease at 26°C and 90% humidity.

(F) Scatter chart to show the number of disease lesions in Guy11 and two independent $\Delta vts1$ mutants. Horizontal line represents the mean, and the error bar is the standard deviation. Data points are shown from 3 biological replicates in different colors (red, blue, and green).

```

S_cerevisiae      -----SILNDDVLKYTKLKIETLTNTPFIS---PPLPAIASPINNRD-----DTQII
M_oryzae         G--QADMLANATAMKLAAMSTVNNRFALDDVRKYRRTRSNDNS--GQ---NPLSPGM--ISP--NVVMVDEHGRV
G_tritici        GVGQADMLANATAMKLAAMSTVNNRFALDDVRKYRRTARSNDAPGNGQ---GGLSPGM--QVPGANVVMIDEHGRV
N_crassa         QGNNADMVANATAMKLAALSTVNNRFALDDARRYRRARSNDGAPGQSHAQHPLSPGPGQ--GIPSTNVVMINEHGQVI
V_dahliae       GGSQADMLANATAMKLAALSTVNNRFALDDVRKYRRTARSNDAPGGPMSAGLTPGQQGV--NIPGTNVVMINEHGQVI
C_chlorophyti   NGTQADMVANATAMKLAALSTVNNRFALDDVRKYRRTARSNDAPGAPGQQHQPQNLQGGV--NLPGANVVMINEHGQVI
C_sublineola    SGTQADMVANATAMKLAALSTVNNRFALDDVRKYRRTARSNDAPGAPGQQGMPQGAQGV--NVPGANVVMINEHGQVI
T_lentiforme    --GQADMVANATAMKLAALSTVNNRFALDDVRKYRRTARSNDAPGAQHOMP--PTFSH--NIPANVVMINEHGQII
F_mangiferae   GGNQADMVANATAMKLAALSTVNNRFALDDVRKYRRTRSNDGTPGQNPVSV-GPCPGI--NLPNTNVVMINEHGQVI
F_oxysporum    GGNQADMVANATAMKLAALSTVNNRFALDDVRKYRRTRSNDGTPGQNPVSA-GPCPGI--NLPNTNVVMINEHGQVI
  
```



```

S_cerevisiae      1-----MKHPYEEFPTGSKSPYNMSRGAHPG-----AVLLSPOSSAIIKNNPG
M_oryzae         126IEQWFRVLSEAERTAALYALLQQTTQVQIRFFIQVLQQMGKNHPM---SGVLSPANFDK---DPMSNRLSDAMNKLSV-
G_tritici        125IEQWFRVLSEAERTAALYALLQQTTQVQIRFFIQVLQQMGKNHPM---SGVLSPASFDK---DPMSNRLSDAMNKLNVG-
N_crassa         117IEQWFRVLSEAERTAALYALLQQTTQVQIRFFIQVLQQMGKNHPM---SGVLSPANFDK---DPMSSRLSDAMGKLEV-
V_dahliae       115IEQWFRVLSEAERTAALYALLQQTTQVQIRFFIQVLQQMGKSHPM---SGVLSPANFDKGEPATSESPPPLDPMSNRLSDAMNKLNV-
C_chlorophyti   115IEQWFRVLSEAERTAALYALLQQTTQVQIRFFIQILQQMGKNHPM---SGVLSPANFDK---DPMSNRLSDAMNKLNV-
C_sublineola    114IEQWFRVLSEAERTAALYALLQQTTQVQIRFFIQVLQQMGKNHPM---SGVLSPANFDK---DPMSNRLSDAMNKLNV-
T_lentiforme    115IEQWFRVLSEAERTAALYALLQQTTQVQIRFFIQVLQQMGKNHPM---SGVLSPATFDK---DPMSSRLSDAMNKLNV-
F_mangiferae   115IEQWFRVLSEAERTAALYALLQQTTQVQIRFFIQVLQQMGKNHPM---SGVLSPASFDK---DPMSNRLSDAMNKLNV-
F_oxysporum    115IEQWFRVLSEAERTAALYALLQQTTQVQIRFFIQVLQQMGKNHPM---SGVLSPASFDK---DPMSNRLSDAMNKLNV-
  
```

Figure S7. The Vts1 S175 residue is present in a conserved region among filamentous fungi, related to Figure 6C

Schematic representation to show arrangement of each phosphorylation site identified for Vts1 and its conservation. Alignments of neighboring regions surrounding Vts1 S175 and S420 from different filamentous fungi were carried out using ClustalX.